The c2d *Spitzer* spectroscopic survey of ices around low-mass young stellar objects. IV. NH$_3$ and CH$_3$OH

Sandrine Bottinelli[1,2,3], A. C. Adwin Boogert[4], Jordy Bouwman[5], Martha Beckwith[5,6],

Ewine F. van Dishoeck[1,7], Karin I. Öberg[5,8], Klaus M. Pontoppidan[9], Harold Linnartz[5],

Geoffrey A. Blake[9], Neal J. Evans II[10], Fred Lahuis[11,1]

– 2 –

[1]Leiden Observatory, Leiden University, P.O. Box 9513, NL 2300 RA Leiden, The Netherlands.

sandrine@strw.leidenuniv.nl

[2]Present address: Centre d'Etude Spatiale des Rayonnements (CESR), UMR 5187, 9 avenue du Colonel Roche, BP 4346, 31028 Toulouse Cedex 4, France.

[3]CESR, Université de Toulouse [UPS], France

[4]IPAC, NASA Herschel Science Center, Mail Code 100-22, California Institute of Technology, Pasadena, CA 91125, USA.

[5]Raymond and Beverly Sackler Laboratory for Astrophysics, Leiden Observatory, Leiden University, P.O. Box 9513, NL 2300 RA Leiden, the Netherlands.

[6]Present address: Department of Chemistry and Chemical Biology, Cornell University, Ithaca, New York 14853

[7]Max-Planck Institute für Extraterrestrische Physik, Giessenbachstr. 1, D-85748 Garching, Germany

[8]Present address: Harvard-Smithsonian Center for Astrophysics, 60 Garden Street, Cambridge, MA 02138, USA

[9]California Institute of Technology, Division of Geological and Planetary Sciences, Pasadena, CA 91125, USA.

[10]Department of Astronomy, University of Texas at Austin, 1 University Station C1400, Austin, TX 78712-0259, USA.

[11]SRON Netherlands Institute for Space Research, PO Box 800, NL 9700 AV Groningen, The Netherlands.

ABSTRACT

NH_3 and CH_3OH are key molecules in astrochemical networks leading to the formation of more complex N- and O-bearing molecules, such as CH_3CN and CH_3OCH_3. Despite a number of recent studies, little is known about their abundances in the solid state. This is particularly the case for low-mass protostars, for which only the launch of the *Spitzer* Space Telescope has permitted high sensitivity observations of the ices around these objects. In this work, we investigate the $\sim 8 - 10$ μm region in the *Spitzer* IRS (InfraRed Spectrograph) spectra of 41 low-mass young stellar objects (YSOs). These data are part of a survey of interstellar ices in a sample of low-mass YSOs studied in earlier papers in this series. We used both an empirical and a local continuum method to correct for the contribution from the 10 μm silicate absorption in the recorded spectra. In addition, we conducted a systematic laboratory study of NH_3- and CH_3OH-containing ices to help interpret the astronomical spectra. We detected the NH_3 ν_2 umbrella mode at $\sim$9 μm in low-mass YSOs for the first time. We identified this feature in 24 sources, with abundances with respect to water between $\sim$2 and 15%. Simultaneously, we also revisited the case of CH_3OH ice by studying the ν_4 C–O stretch mode of this molecule at $\sim$9.7 μm in 16 objects, yielding abundances consistent with those derived by Boogert et al. (2008) (hereafter paper I) based on a simultaneous 9.75 and 3.53 μm data analysis. Our study indicates that NH_3 is present primarily in H_2O-rich ices, but that in some cases, such ices are insufficient to explain the observed narrow FWHM. The laboratory data point to CH_3OH being in an almost pure methanol ice, or mixed mainly with CO or CO_2, consistent with its formation through hydrogenation on grains. Finally, we use our derived NH_3 abundances in combination with previously published abundances of other solid N-bearing species to find that up to 10–20 % of nitrogen is

locked up in known ices.

Subject headings: infrared: ISM — ISM: molecules — ISM: abundances — stars: formation — astrochemistry

1. Introduction

Ammonia and methanol are among the most ubiquitous and abundant (after H_2 and CO) molecules in space. Gaseous NH_3 and CH_3OH are found in a variety of environments such as infrared dark clouds, dense gas surrounding ultra-compact H II regions, massive hot cores, hot corinos, and comets. Solid CH_3OH has been observed in the ices surrounding massive YSOs (e.g. Schutte et al. 1991; Dartois et al. 1999; Gibb et al. 2004) and more recently toward low-mass protostars (Pontoppidan et al. 2003). The presence of solid NH_3 has been claimed toward massive YSOs only (Lacy et al. 1998; Dartois et al. 2002; Gibb et al. 2004; Gürtler et al. 2002), with the exception of a possible detection in the low-mass object IRAS 03445+3242 (Gürtler et al. 2002). However, these detections are still controversial and ambiguous (Taban et al. 2003).

Both molecules are key participants in gas-grain chemical networks resulting in the formation of more complex N- and O-bearing molecules, such as CH_3CN and CH_3OCH_3 (e.g. Rodgers & Charnley 2001). Moreover, UV processing of NH_3- and CH_3OH-containing ices has been proposed as a way to produce amino-acids and other complex organic molecules (e.g., Muñoz Caro & Schutte 2003; Bernstein et al. 2002; Öberg et al. 2009). In addition, the amount of NH_3 in ices has a direct impact on the content of ions such as NH_4^+ and OCN^-, which form reactive intermediates in solid-state chemical networks. A better knowledge of the NH_3 and CH_3OH content in interstellar ices will thus help to constrain chemical models and to gain a better understanding of the formation of more complex, prebiotic, molecules.

During the pre-stellar phase, NH_3 is known to freeze out on grains (if the core remains starless long enough – Lee et al. 2004). Moreover, CH_3OH is known to have gas-phase abundances with respect to H_2 in hot cores/corinos that are much larger than in cold dense clouds: $\sim (1 - 10) \times 10^{-6}$ vs $\leq 10^{-7}$, with the former values most likely representing

evaporated ices in warm regions (e.g. Genzel et al. 1982; Blake et al. 1987; Federman et al. 1990). Together, these findings suggest that ices are an important reservoir of NH_3 and CH_3OH and that prominent features should be seen in the absorption spectra toward high- and low-mass protostars. Unfortunately, as summarized in Table 1, NH_3 and CH_3OH bands, with the exception of the 3.53 μm CH_3OH feature, are often blended with deep water and/or silicate absorptions, complicating unambiguous identifications and column density measurements. This is particularly true for NH_3 whose abundance determination based on the presence of an ammonium hydrate feature at 3.47 μm remains controversial (e.g. Dartois & d'Hendecourt 2001). Nonetheless, it is important to use all available constraints to accurately determine the abundances of these two molecules. Despite the overlap with the 10 μm silicate (Si–O stretch) feature, the NH_3 ν_2 umbrella mode at $\sim$9 μm ($\sim$1110 cm^{-1}) offers a strong intrinsic absorption cross section and appears as the most promising feature to determine the abundance of this species in the solid phase. Moreover, the CH_3OH ν_4 C–O stretch at $\sim$9.7 μm ($\sim$1030 cm^{-1}) provides a good check on the validity of the different methods we will use to subtract the 10-μm silicate absorption, since the abundance of this molecule has been accurately determined previously from both the 3.53 and 9.75 μm features (see Paper I).

More detailed spectroscopic information is particularly interesting for low-mass protostars as the ice composition reflects the conditions during the formation of Sun-like stars. Such detections have only become possible with *Spitzer*, whose sensitivity is necessary to observe low luminosity objects even in the nearest star-forming clouds.

The gain in sensitivity and spectral resolution offered by *Spitzer* implies that the interpretation of the astronomical spectra should be supported by a systematic laboratory study of interstellar ice analogues containing NH_3 and CH_3OH. The spectral appearance of ice absorption features, such as band shape, band position and integrated band strength,

Table 1.   Selected near- and mid-infrared features of NH_3 and CH_3OH.

Mode	λ (μm)	$\bar{\nu}$ (cm^{-1})	Problem
NH_3 features:			
ν_3 N–H stretch	2.96	3375	Blended with H_2O (O–H stretch, 3.05 μm/3275 cm^{-1})
ν_4 H–N–H bend	6.16	1624	Blended with H_2O (H–O–H bend, 5.99 μm/1670 cm^{-1}), HCOOH
ν_2 umbrella	**9.00**	**1110**	**Blended with silicate**
CH_3OH features:			
ν_2 C–H stretch	3.53	2827	–
ν_6 & ν_3 –CH$_3$ deformation	6.85	1460	Blended (e.g. with NH_4^+)
ν_7 –CH$_3$ rock	8.87	1128	Weak; blended with silicate
ν_4 C–O stretch	**9.75**	**1026**	**Blended with silicate**
Torsion	14.39	695	Blended with H_2O libration mode

Note. — The bold-faced lines indicate the features studied here.

Note. — The nomenclature for the NH_3 and CH_3OH vibrational modes are adopted from Herzberg (1945).

is rather sensitive to the molecular environment. Changes in the lattice geometry and physical conditions of an ice are directly reflected by variations in these spectral properties. In the laboratory, it is possible to record dependencies over a wide range of astrophysically relevant parameters, most obviously ice composition, mixing ratios, and temperature. Such laboratory data exist for pure and some H_2O-rich NH_3- and CH_3OH-containing ices (e.g., d'Hendecourt & Allamandola 1986; Hudgins et al. 1993; Kerkhof et al. 1999; Taban et al. 2003), but a systematic study and comparison with observational spectra is lacking.

In principle, the molecular environment also provides information on the formation pathway of the molecule. For example, NH_3 ice is expected to form simultaneously with H_2O and CH_4 ice in the early, low-density molecular cloud phase from hydrogenation of N atoms (e.g., Tielens & Hagen 1982). In contrast, solid CH_3OH is thought to result primarily from hydrogenation of solid CO, a process which has been confirmed to be rapid at low temperatures in several laboratory experiments (e.g. Watanabe & Kouchi 2002; Hidaka et al. 2004; Fuchs et al. 2009). A separate, water-poor layer of CO ice is often found on top of the water-rich ice layer in low-mass star-forming regions due to the 'catastrophic' freeze-out of gas-phase CO at high densities (Pontoppidan et al. 2003; Pontoppidan 2006). Hydrogenation of this CO layer should lead to a nearly pure CH_3OH ice layer (e.g., Cuppen et al. 2009), which will have a different spectroscopic signature from that of CH_3OH embedded in a water-rich matrix. The latter signature would be expected if CH_3OH ice were formed by hydrogenation of CO in a water-rich environment or by photoprocessing of H_2O:CO ice mixtures, another proposed route (e.g., Moore & Hudson 1998).

Here, we present *Spitzer* spectra between 5 and 35 μm of ices surrounding 41 low-mass protostars, focusing on the $\sim 8 - 10$ μm region that contains the ν_2 umbrella and ν_4 C–O stretch modes of NH_3 and CH_3OH, respectively. This work is the fourth paper in a series of ice studies (Boogert et al. 2008; Pontoppidan et al. 2008; Öberg et al. 2008) carried out

in the context of the *Spitzer* Legacy Program "From Molecular Cores to Planet-Forming Disks" ("c2d"; Evans et al. 2003). In Section 2, we carry out the analysis of the *Spitzer* data in $8 - 10$ μm range. In Section 3, we present the laboratory data specifically obtained to help interpret the data that are discussed in Section 4. Finally, we conclude in Section 5 with a short discussion of the joint astronomy-laboratory work (including the overall continuum determination).

2. Astronomical observations and analysis

The source sample consists of 41 low-mass YSOs that were selected based on the presence of ice absorption features. The entire sample spans a wide range of spectral indices $\alpha = -0.25$ to $+2.70$, with α defined as $d \log(\lambda F_\lambda)/d \log(\lambda)$, where d indicates the derivative, and F_λ represents all the photometric fluxes available between $\lambda = 2.17$ μm (2MASS K_s-band) and $\lambda = 24$ μm (*Spitzer*/MIPS band). In the infrared broad-band classification scheme, 35 out of 41 objects fall in the embedded Class 0/I category ($\alpha > 0.3$). The remaining 6 objects are flat-spectrum type objects ($-0.3 < \alpha < 0.3$; Greene et al. 1994). *Spitzer*/IRS spectra (5-35 μm) were obtained as part of the c2d Legacy program (PIDs 172 and 179), as well as a dedicated open time program (PID 20604), and several previously published GTO spectra (Watson et al. 2004). We refer the reader to Table 1 and Section 3 of Boogert et al. (2008) for the source coordinates and a description of the data reduction process (including overall continuum determination).

As mentioned previously, spectral signatures in the $\sim 8 - 10$ μm region are dominated by the Si–O stretching mode of silicates. The overall shape as well as the sub-structure of the silicate feature depend on grain size, mineralogy, level of crystallinity. These effects are degenerate and so these different factors cannot be easily separated. For example, large

grains and the presence of SiC both produce a shoulder at 11.2 μm (e.g., Min et al. 2007). Therefore, trying to fit the 10 μm silicate feature by determining the composition and size of the grains is a complex process. For this reason, we use two alternative methods to model the silicate profile and extract the NH_3 (and CH_3OH) feature(s) from the underlying silicate absorption.

2.1.   Local continuum

The first method uses a local continuum to fit the shape of the silicate absorption. For this, we fit a fourth order polynomial over the wavelength ranges 8.25–8.75, 9.23–9.37, and 9.98–10.4 μm, avoiding the positions where NH_3 and CH_3OH absorb around 9 and 9.7 μm. These fits are shown with thick black lines in Fig. 1. After subtraction of the local continuum from the observations, we fit a Gaussian to the remaining NH_3 and/or CH_3OH feature, when present, as shown in Fig. 2. The results of the Gaussian fits are listed in Table A.1 of Appendix A.

2.2.   Template

The second method assumes that the 8–10 μm continuum can be represented by a template silicate absorption feature, selected among the observed sources. A comparison of the results obtained using a template to those obtained using a simple local continuum provides an estimate of the influence of the continuum choice on the shape and depth of the NH_3 and CH_3OH features. The templates were chosen using an empirical method. Upon examination of the 10 μm feature of the entire sample, the sources could be separated into three general categories, depending on the shape of the wing of the silicate absorption between $\sim$8 and 8.7 μm (which we will refer to as the 8 μm wing): (i) sources with a

– 11 –

straight 8 μm wing (Fig. 3-a), (ii) sources with a curved 8 μm wing (Fig. 3-b), and (iii) sources with a rising 8 μm wing ("emission" sources, Fig. 3-c).

Note that, since radiative transfer in the 8–10 μm region can be complicated by the presence of silicate emission, we only consider sources that are the least affected by emission, that is those falling in one of the first two categories. Nevertheless, non-rising silicate profiles might still suffer from the presence of emission. To try and estimate the impact of this potential effect, we used two silicate emission sources from Kessler-Silacci et al. (2006), and subtracted these emission profiles from our absorption profiles, assuming that the emission represented 10 to 50% of the observed absorption. After removal of a local continuum, we determined the integrated optical depths of the NH_3 and CH_3OH features in the spectra corrected for emission, and compared these to the integrated optical depths of the uncorrected spectra. We find that the difference can be up to a factor of two and therefore identify this possible presence of underlying emission as the largest source of uncertainty in our abundance determinations.

For each of the straight and curved 8 μm wings, two sources (in order to test for template-dependent effects) were selected as possible templates for the silicate feature. The selection criteria were: (i) a silicate feature as deep as possible to minimize the effects of silicate emission and (ii) little NH_3 and CH_3OH signal, as estimated after subtraction of a local continuum. Additionally, we added to this list the GCS3 spectrum observed by Kemper et al. (2004) toward the Galactic Center. The spectra of these templates in the 8–10 μm region are displayed in Fig. 4.

For all the other sources in our sample, the best template was determined by scaling the possible templates to the observed optical depth at different wavelengths (8.75, 9.30, 9.37, 9.70, 9.98 μm) and finding the combination (template+scaling point) that gave the least residuals over the same wavelength ranges used to estimate the local continuum

(8.25–8.75, 9.23–9.37, 9.98–10.4 μm). The result of this process is displayed for each source in the top part of Fig. 1, where the best template is shown by a grey line. The bottom panels of Fig. 1 show sources for which no reasonable template could be found, as well as emission sources, in which case only the local continuum is overlaid. As in the case of the local continuum method, the spectra obtained after subtraction of the templates are shown in Fig. 2. Taken together, NH$_3$ features are detected in 24 out of 41 sources.

The top panel of Figure 2 shows that the CH$_3$OH feature is not affected by the continuum choice, whereas the width of the NH$_3$ band is somewhat sensitive to this choice, especially if there is no CH$_3$OH absorption, in which case the local continuum yields a wider NH$_3$ profile. For both continua, NH$_3$ ice is unambiguously identified.

2.3. NH$_3$ ice column densities and abundances

Gaussian fits were performed to the NH$_3$ and/or CH$_3$OH features when present, and derived parameters for NH$_3$ are listed in Table A.1 (Appendix A). Table 2 gives the column densities derived for NH$_3$ for each of the two methods employed to determine the continuum, using a band strength of 1.3×10^{-17} cm molecule^{-1} for the NH$_3$ ν_2 umbrella mode appropriate for a water-rich ice (d'Hendecourt & Allamandola 1986; Kerkhof et al. 1999). The two methods generally agree to within a factor of 2 or better. A similar factor of ≤2 overall uncertainty is estimated for those sources for which only the local continuum has been used.

The position of the NH$_3$ ν_2 umbrella mode is very close to that of the ν_7 CH$_3$-rock mode of CH$_3$OH. As illustrated by our laboratory data (see Section 3), sources with an absorption depth at $\sim$9.7 μm (CO-stretch mode of CH$_3$OH) at least twice as large as the absorption depth at $\sim$9 μm (blend of CH$_3$-rock mode of CH$_3$OH and NH$_3$ umbrella

mode) have a significant contribution to the 9-μm integrated optical depth from the CH$_3$-rock mode of CH$_3$OH. In these cases (sources followed by an asterisk in Table 2 and in Table A.1 of Appendix A), we performed the following correction: we scaled a H$_2$O:CH$_3$OH=9:1 laboratory spectrum to the observed optical depth of the CO-stretch mode of CH$_3$OH, determined the integrated optical depth of the CH$_3$-rock mode of CH$_3$OH in that scaled spectrum, and subtracted it from the total observed optical depth at 9 μm. This correction is justified by the fact that the H$_2$O:CH$_3$OH:NH$_3$=10:4:1 spectrum, a typical interstellar abundance mixture, is well reproduced around 8–10 μm by a combination of H$_2$O:CH$_3$OH=9:1 and H$_2$O:NH$_3$=9:1 (see Sec. 3).

The inferred NH$_3$ ice abundances range from $\lesssim$ 1% to 15% with an average of 5.5±2%, with respect to H$_2$O ice. Excluding the abnormally high value of EC82, this relative abundance is centered on 5.5% with a standard deviation of 2.0%. This is similar to what was obtained by Öberg et al. (2008) for CH$_4$, another ice component that should form via hydrogenation. For 6 out of the 8 sources where both NH$_3$ and CH$_4$ are detected, the NH$_3$-to-CH$_4$ ratio is slightly larger than 1 ($\sim$1.2). Based on elemental abundance ratios, one would expect NH$_3$/CH$_4$ smaller than 1, but since two thirds of the carbon is in refractory grains and some fraction of the gaseous CO locked up in CO at the ice formation threshold, NH$_3$-to-CH$_4$ ratios larger than 1 are consistent with both NH$_3$ and CH$_4$ being formed by hydrogenation of N and C, respectively.

Here, we only report values for the Gaussian parameters and derived column densities in the appendix (see Table A.2), to show that the numbers we obtain in this independent study are consistent with those reported in Paper I. Our recommended abundances are those from paper I, based on the combined 9.75 and 3.53 μm analysis. The inferred CH$_3$OH abundances range from < 1% to > 25% with respect to H$_2$O ice, indicating significant CH$_3$OH/NH$_3$ abundance variations from source-to-source. Such relative abundance

variations can already be clearly seen from the changing relative depths of the 9.0 and 9.7 μm features (see also Paper I). Thus, NH$_3$ and CH$_3$OH ice are likely formed through different formation pathways and/or in different ice environments.
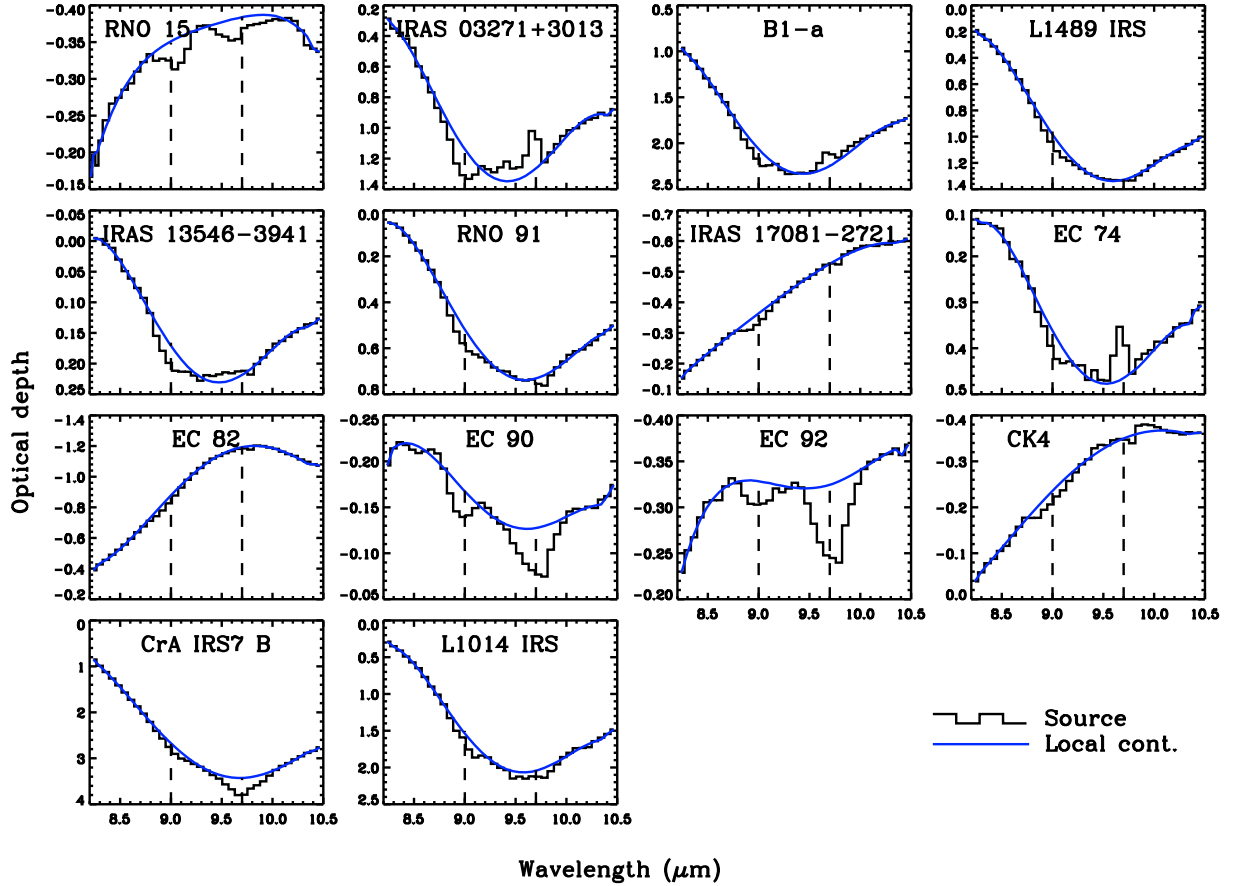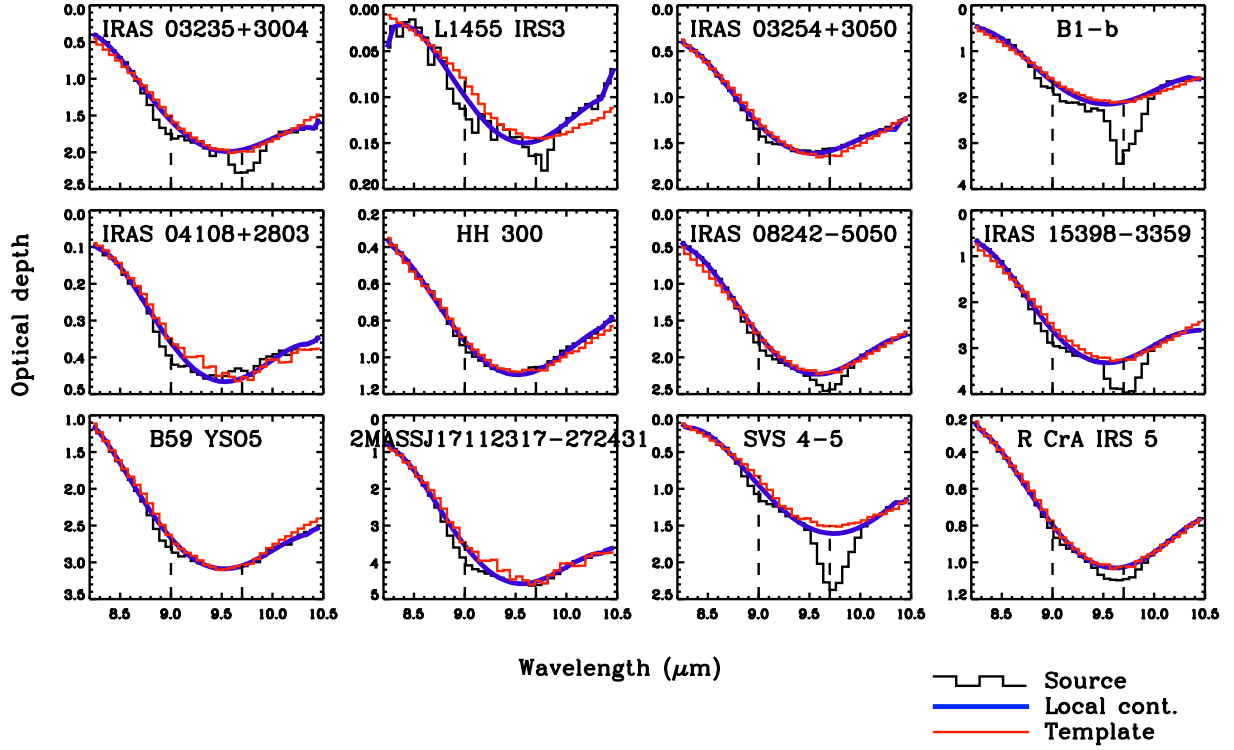
Fig. 1.— (*Top*) Local continuum (thick blue/black lines) and template (red/grey lines) fits
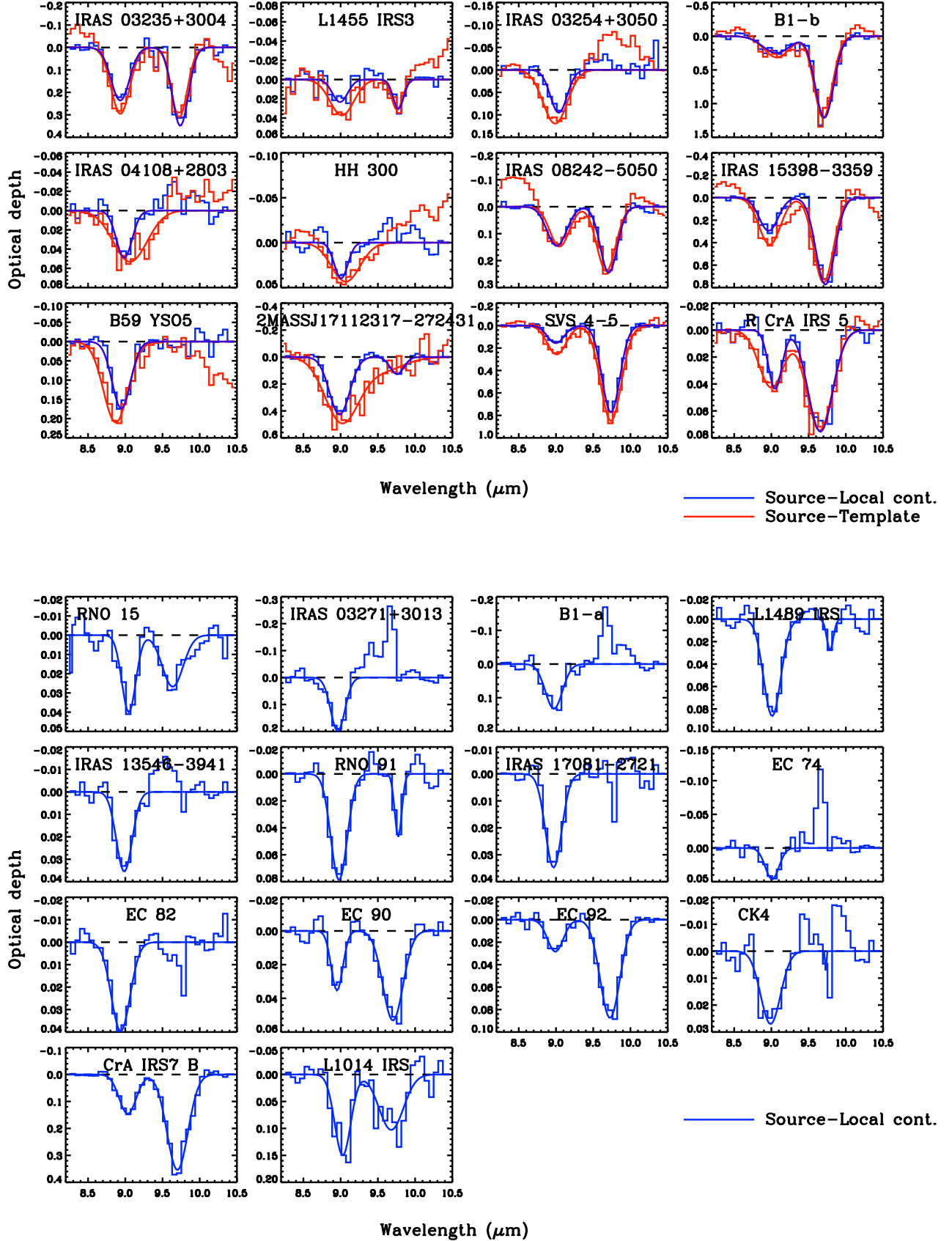
Fig. 2.— (*Top*) Residual after removal of local continuum and template fits for all sources for which a template could be found. (See Section 2.2 for details) — (*Bottom*) Residual after removal of local continuum fits for emission sources or sources for which no reasonable
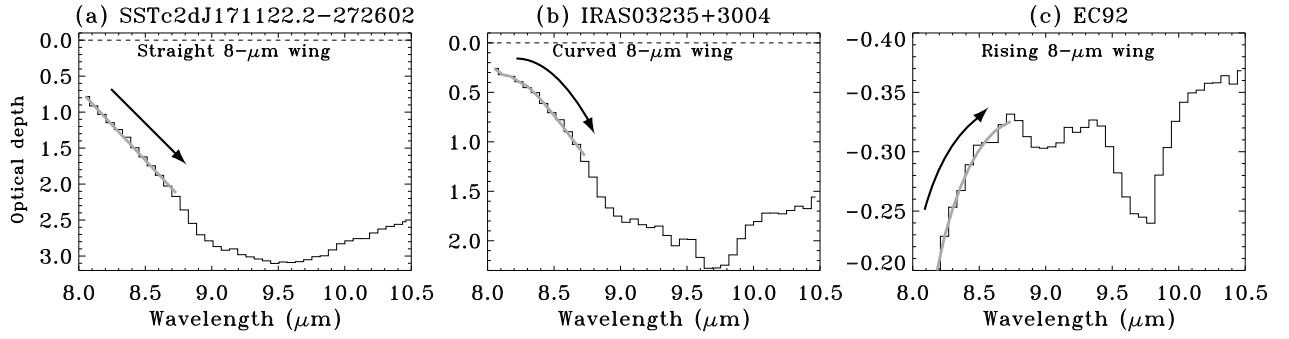
Fig. 3.— Examples illustrating the three shapes of the 8 μm wing shown by the thick grey line: (a) straight, (b) curved, and (c) rising.
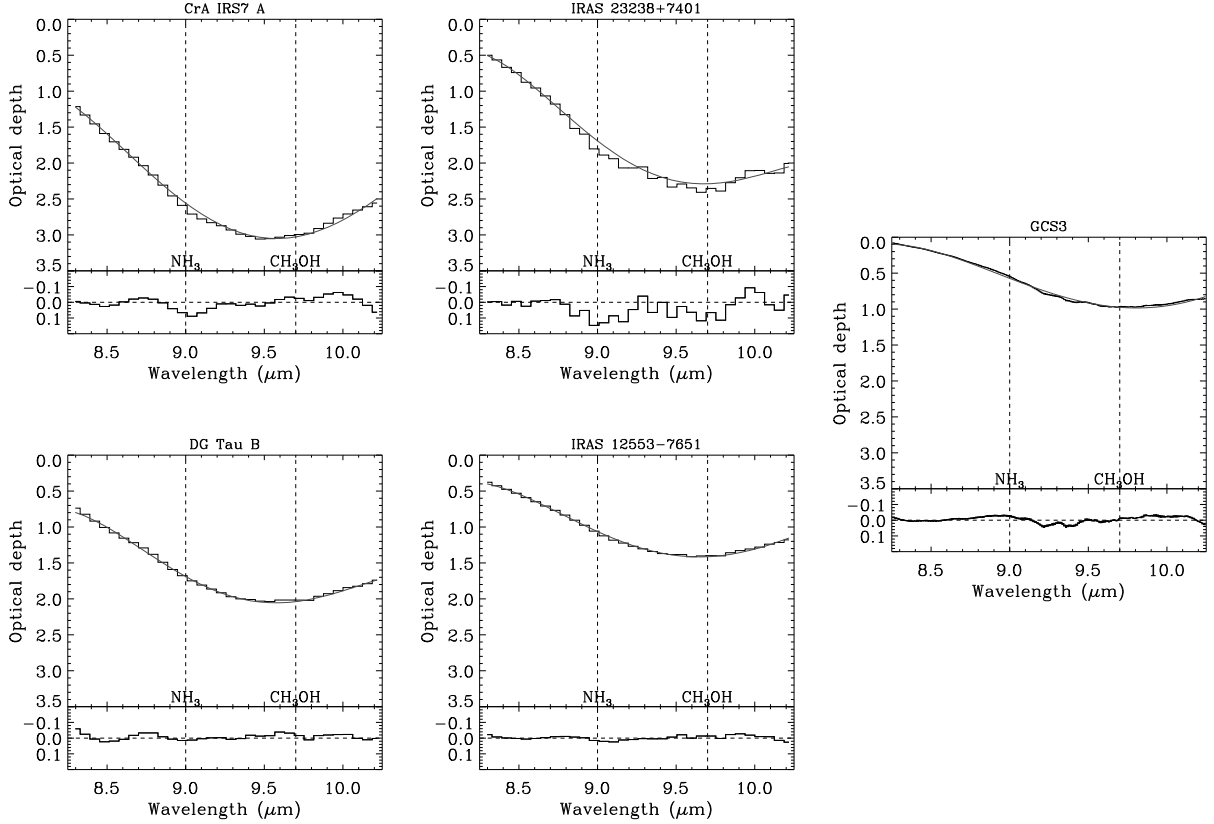
Fig. 4.— Silicate features of the sources used as templates for a straight 8 μm wing (left), curved 8-μm wing (middle), and GCS3 (right). The bottom panels of each plot are the residuals after removal of the local continuum shown in grey in the top panels. The optical depth scale is kept fixed for comparison. These sources are selected to have no or at most weak NH_3 and CH_3OH absorptions.

Table 2.   NH$_3$ column densities[a] and abundances with respect to H$_2$O ice[b]

Source	NH$_3$, local		NH$_3$, template		Template	Scaling point
	$\times 10^{17}$ cm^{-2}	% H$_2$O[b]	$\times 10^{17}$ cm^{-2}	% H$_2$O[b]		μm
IRAS 03235+3004	6.83 (0.98)	4.71 (1.00)	8.94 (1.03)	6.17 (1.20)	IRAS 12553	9.30
L1455 IRS3	0.57 (0.23)	6.21 (3.51)	1.41 (0.27)	15.37 (6.86)	GCS3	9.37
IRAS 03254+3050	2.44 (0.39)	6.66 (1.37)	4.58 (0.49)	12.52 (2.10)	IRAS 12553	10.40
B1-b*	∼7.3	∼4.2	∼9.8	∼5.6	IRAS 12553	9.70
IRAS 04108+2803	1.23 (0.24)	4.29 (1.03)	2.07 (0.39)	7.21 (1.69)	IRAS 23238	9.70
HH 300	0.90 (0.22)	3.46 (0.90)	2.23 (0.37)	8.60 (1.65)	DG Tau B	9.70
IRAS 08242−5050	4.77 (0.46)	6.13 (0.85)	4.41 (0.54)	5.66 (0.89)	IRAS 12553	9.70
IRAS 15398−3359	8.73 (1.18)	5.90 (1.77)	13.80 (1.35)	9.33 (2.65)	IRAS 12553	9.70
B59 YSO5	4.92 (0.72)	3.53 (0.88)	6.37 (0.99)	4.57 (1.17)	CrA IRS7 A	9.70
2MASSJ17112317−272431	13.10 (1.06)	6.70 (0.54)	20.60 (2.76)	10.58 (1.42)	IRAS 23238	9.70
SVS 4-5*	∼2.4	∼4.3	∼5.8	∼10.3	GCS3	8.75
R CrA IRS 5	0.91 (0.23)	2.54 (0.67)	1.49 (0.31)	4.15 (0.92)	IRAS 12553	9.70
RNO 15[c]	0.80 (0.21)	11.58 (3.18)	–	–	–	–
IRAS 03271+3013	4.90 (0.88)	6.37 (1.86)	–	–	–	–
B1-a	3.46 (0.69)	3.33 (0.98)	–	–	–	–
L1489 IRS	2.31 (0.30)	5.42 (0.96)	–	–	–	–
IRAS 13546−3941	0.94 (0.16)	4.56 (0.87)	–	–	–	–
RNO 91	2.03 (0.30)	4.78 (0.81)	–	–	–	–
IRAS 17081−2721	0.86 (0.16)	6.54 (1.39)	–	–	–	–
EC 74[c]	1.00 (0.29)	9.35 (3.13)	–	–	–	–
EC 82	1.22 (0.14)	31.31 (6.65)	–	–	–	–
EC 90	0.67 (0.20)	3.94 (1.24)	–	–	–	–
EC 92*	∼0.5	∼3.0	–	–	–	–
CrA IRS7 B*	∼3.0	∼2.8	–	–	–	–
L1014 IRS	3.72 (0.91)	5.20 (1.43)	–	–	–	–
CK4	0.84 (0.13)	5.37 (0.86)	–	–	–	–
3-σ upper limits						
LDN 1448 IRS1	0.20	4.15	–	–	–	–
IRAS 03245+3002	17.28	4.40	–	–	–	–
L1455 SMM1	15.10	8.29	–	–	–	–
IRAS 03301+3111	0.24	5.93	–	–	–	–

Table 2—Continued

Source	NH$_3$, local		NH$_3$, template		Template	Scaling point
	$\times 10^{17}$ cm^{-2}	% H$_2$O^b	$\times 10^{17}$ cm^{-2}	% H$_2$O^b		μm
B1-c	11.93	4.04	–	–	–	–
IRAS 03439+3233	0.31	3.10	–	–	–	–
IRAS 03445+3242	0.47	2.09	–	–	–	–
DG Tau B	0.47	2.05	–	–	–	–
IRAS 12553-7651	0.61	2.04	–	–	–	–
Elias 29	0.28	0.93	–	–	–	–
CRBR 2422.8−342	0.52	1.23	–	–	–	–
HH 100 IRS	0.46	1.89	–	–	–	–
CrA IRS7 A	0.97	0.89	–	–	–	–
CrA IRAS32	5.44	10.35	–	–	–	–
IRAS 23238+7401	1.60	1.24	–	–	–	–

Note. — Sources in bold were used as templates. Uncertainties quoted in parenthesis are statistical errors from the Gaussian fits while absolute errors are up to a factor of 2.

[a] Derived using a bandstrength of 1.3×10^{-17} cm molecule^{-1}.

[b] Using the H$_2$O ice column densities listed in Paper I.

[c] Values are likely upper limits (see Section 4.2 for details).

[*] Sources with $\tau_{9.7\mu m} > 2 \times \tau_{9.0\mu m}$, for which an estimated contribution from the CH$_3$-rock mode of CH$_3$OH was subtracted (see text for details).

3.   Laboratory work and analysis

The band profiles presented in Fig. 2 contain information on the ice environment in which NH_3 and CH_3OH are located, and thus their formation and processing history. To extract this information, a systematic laboratory study of the NH_3 and CH_3OH features in a variety of ices has been carried out. Specifically, three features between 8 and 10 μm have been analyzed:

1. the NH_3 ν_2 umbrella mode, at $\sim$9.35 μm or 1070 cm^{-1} in pure NH_3 ice, and with band strength A_{pure} =1.7×10^{-17} cm molecule^{-1} (d'Hendecourt & Allamandola 1986),

2. the CH_3OH ν_4 CO– stretching mode, at $\sim$9.74 μm or 1027 cm^{-1} in pure CH_3OH ice, and with $A_{\mathrm{pure}} = 1.8$×10^{-17} cm molecule^{-1} (d'Hendecourt & Allamandola 1986),

3. the CH_3OH ν_7 CH_3 rocking mode, at $\sim$8.87 μm or 1128 cm^{-1} in pure CH_3OH ice, and with $A_{\mathrm{pure}} = 1.8$×10^{-18} cm molecule^{-1} (Hudgins et al. 1993).

It should be noted that, as mentioned in the above list, the quoted positions are for pure ices only and therefore slightly deviate from the astronomical values given in Table 1.

This laboratory study targeted pure, binary and tertiary interstellar ice analogs consisting of different mixtures of H_2O, NH_3, CH_3OH, CO and CO_2, the major ice components. All measurements were performed under high vacuum conditions ($\sim 10^{-7}$ mbar) using an experimental approach described in Gerakines et al. (1995), Bouwman et al. (2007) and Öberg et al. (2007). The ice spectra were recorded in transmission using a Fourier transform infrared spectrometer covering 25–2.5 μm (400–4000 cm^{-1}) with 1 cm^{-1} resolution and by sampling relatively thick ices,

typically several thousands Langmuir[1] (L) thick. These ices were grown at a speed of $\sim 10^{16}$ molecules cm^{-2} s^{-1} on a temperature-controlled CsI window.

A typical reduced spectrum for an ice mixture containing H$_2$O:CH$_3$OH:NH$_3$= 10:4:1 at 15 K is shown in Fig. 5. Since band profiles and strengths change with ice composition and also with temperature, the three fundamentals mentioned above were investigated as a function of temperature ranging from 15 to 140 K with regular temperature steps for a number of binary and tertiary mixtures (listed in Appendix B). An IDL routine was used to determine the location of the band maximum, FWHM and integrated absorbance of the individual absorption bands. For the asymmetric NH$_3$ ν_2 umbrella mode the band position has been determined by the maximum absorbance and for the symmetric profiles the spectral parameters have been determined from Gaussian fits of baseline subtracted spectra. The resulting absolute frequency uncertainty is of the order of 1 cm^{-1}. The measurements are presented in Table B.3 of Appendix B, and are included in the Leiden laboratory database[2].

NH$_3$ and CH$_3$OH both have the ability to form hydrogen bonds in water-rich matrices, so it is not surprising that the band profile changes compared with pure ices because of the various molecular interactions (e.g., d'Hendecourt & Allamandola 1986)

In addition to profiles, band strengths can change with environment and with temperature, as discussed for the cases of CO and CO$_2$ in water-rich ices in Kerkhof et al. (1999); Öberg et al. (2007); Bouwman et al. (2007). Figure 6 shows how the NH$_3$ ν_2

---

[1]One Langmuir corresponds to a pressure of 10^{-6} torr for 1 second and measures the exposure of a surface to adsorption of gases. One Langmuir is equivalent to about 10^{15} molecules cm^{-2}.

[2]http://www.strw.leidenuniv.nl/~lab/

umbrella mode absorption maximum shifts from 1070 cm^{-1} (9.35 μm) for pure NH_3 ice to 1118 cm^{-1} (8.94 μm) for an astronomically more realistic H_2O:NH_3=9:1 (hereafter 9:1) mixture, for which the FWHM and integrated band strength also change significantly. For example, the band strength is lowered in the 9:1 mixture to 70% of its initial value in pure NH_3 ice. This is in good agreement with previous experiments performed by Kerkhof et al. (1999). The spectral appearance also depends on temperature; for the 9:1 mixture a temperature increase from 15 to 120 K results in a redshift of the peak position from 1118 to 1112 cm^{-1} (8.94 to 8.99 μm) and the FWHM decreases from 62 to 52 cm^{-1} (0.50 to 0.42 μm) (see Fig. 7). The NH_3 bandstrength, on the other hand, does not show any temperature dependence.

If NH_3 is in a water-poor environment with CO and/or CO_2, the ν_2 peak position shifts to the red compared with pure NH_3, to as much as 1062 cm^{-1} (9.41 μm). The FWHM is not much affected whereas the band strength is lowered by 20%. Because of the intrinsically large difference in band maximum position between NH_3 in a water-poor and water-rich environment, the astronomical observations can distinguish between these two scenarios.

Methanol-containing ices have been studied in a similar way (see Fig. 8). The weakly absorbing ν_7 CH_3 rocking mode at $\sim$1125 cm^{-1} (8.89 μm) is rather insensitive to H_2O mixing, but the ν_4 CO stretch vibration shifts to the red from 1028 to 1020 cm^{-1} (9.73 to 9.80 μm) when changing from a pure CH_3OH ice to a H_2O:CH_3OH=9:1 mixture. In the latter spectrum the CH_3OH ν_4 CO stretch mode needs to be fitted with a double Gaussians. A substructure appears for a temperature of 80 K (right panel of Fig. 8) while for even higher temperatures, a clearly double peaked structure becomes visible (as previously seen in e.g. Fig. 2 of Schutte et al. 1991). This splitting hints at different physical sites and has been previously ascribed to type II clathrate formation in the ice (Blake et al. 1991).

When CH_3OH is mixed with CO, the band maximum shifts from 1028 to 1034 cm^{-1} (9.73 to 9.67 μm) when going from a 9:1 to a 1:9 CH_3OH:CO mixture. When 50% or more CO is mixed in, the CH_3OH ν_4 CO stretch mode starts to show a shoulder and cannot be fitted correctly by a single Gaussian component (see Fig. 9). Such a two-component profile would not be recognized, however, at the spectral resolution and signal/noise of our *Spitzer* data, so for the comparison between laboratory and observational data a single Gaussian is used. Overall, the shifts of the CH_3OH ν_4 mode between water-rich and CO-rich mixtures are much smaller than in the case of the NH_3 ν_2 mode.

The effect of CH_3OH on the 4.7μm ν_1 stretch mode of CO has also been investigated. The band maximum shifts from 2139 cm^{-1} (4.68 μm) for the nearly pure 9:1 CO:CH_3OH mixture to 2136 and 2135 cm^{-1} for the 1:1 and 1:9 mixtures, respectively. The CO band located at 2136 cm^{-1} is often referred to as CO residing in a polar, mainly H_2O ice, environment. Clearly, the polar CH_3OH molecules can also contribute to CO absorption at 2136 cm^{-1} when intimately mixed in an astronomical ice.

Binary mixtures of NH_3 and CH_3OH have been studied as well. The CH_3OH modes behave very much as they do in a pure methanol ice, but the NH_3 ν_2 umbrella mode is clearly suppressed. Its integrated absorbance is readily reduced to 70% of the integrated absorbance of pure NH_3 in a CH_3OH:NH_3=1:1 mixture and becomes even lower for a 4:1 binary composition. The NH_3 band also broadens compared to pure NH_3 or H_2O:NH_3 mixtures and strongly overlaps with the CO stretching mode of CH_3OH, to the level that it becomes difficult to measure.

A qualitative comparison with the astronomical data (see Section 4) indicates that neither pure NH_3, CH_3OH, nor mixed CH_3OH:NH_3 or H_2O-diluted binary ices can simultaneously explain the different NH_3 profiles in the recorded *Spitzer* spectra. Thus, a series of tertiary mixtures with H_2O:CH_3OH:NH_3 in ratios 10:4:1, 10:1:1 and 10:0.25:1 have

been measured, because CH_3OH is the next major ice component. These ratios roughly span the range of observed interstellar column density ratios. In Fig. 10, the spectra of $H_2O:CH_3OH:NH_3$ tertiary mixtures are plotted and compared to binary $H_2O:CH_3OH$ and $H_2O:NH_3$ data. The NH_3 ν_2 umbrella mode shifts slightly to the blue in the presence of both H_2O and CH_3OH, with an absorption maximum at 1125 cm^{-1} (8.90 μm) for the 10:4:1 $H_2O:CH_3OH:NH_3$ mixture (compared to 1118 cm^{-1} (8.94 μm) in the $H_2O:NH_3$=9:1 mixture). The peak intensity of the NH_3 ν_2 umbrella mode band in this tertiary mixture is small compared with that of the CH_3OH CH_3 rock mode, but its integrated intensity is a factor of two larger because of the larger NH_3 width.

The ν_4 C–O stretching vibration profile of CH_3OH in the tertiary mixture does not differ much from the binary values for the highest water content. The position of the absorption maximum is also only marginally affected by the temperature. The FWHM decreases from 30 cm^{-1} (0.29 μm) for the 10:4:1 mixture to 22 cm^{-1} (0.21 μm) for the 10:0.25:1 mixture.

Besides H_2O, other species may also be regarded as potential candidates for changing the spectral appearance of the NH_3 and/or CH_3OH features. Chemically linked is HCOOH (Bisschop et al. 2007) which unfortunately cannot be deposited in the present setup because of its reactive behavior when mixed with NH_3. Tertiary mixtures with CO and CO_2, two other important constituents in interstellar ices, have been measured (see Appendix B) but here the differences are small compared with the observed binary water-rich or CO-rich mixtures, and do not offer an alternative explanation.
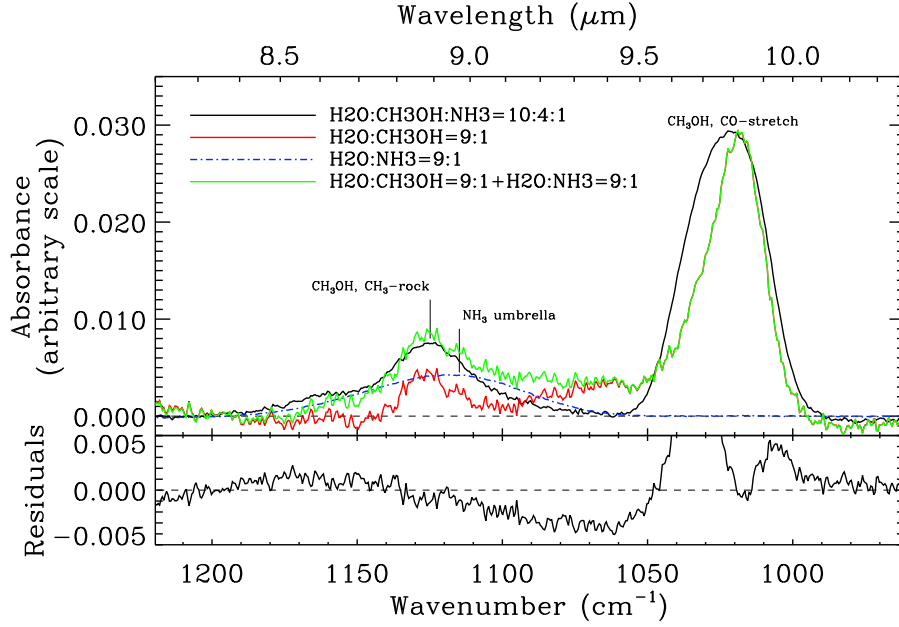
Fig. 5.— Example of a reduced laboratory spectrum (solid black line) for a $H_2O:CH_3OH:NH_3$= 10:4:1 ice mixture at 15 K, in the 8–10 μm / 960–1220 cm^{-1} range. This spectrum can be approximated as the sum (solid green/dark grey line) of $H_2O:CH_3OH$=9:1 (solid red/light grey line) and $H_2O:NH_3$=9:1 (dash-dot blue/grey line). The bottom plot is the difference between the two, showing that the feature at 9 μm (blend of NH_3 and CH_3OH CH_3-rock modes) is well reproduced by the sum of the two individual signatures. This figure also illustrates the fact that the positions of the features in mixed ices differ from that in pure ices (see list at the beginning of this section).
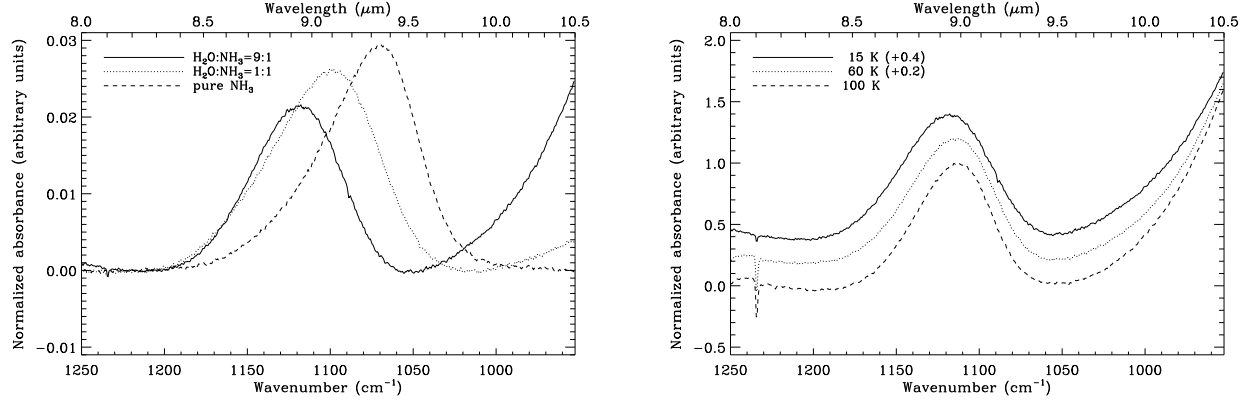
Fig. 6.— (*Left*) FTIR ice spectra of the ν_{NH3} mode for pure NH_3, a H_2O:NH_3=1:1 and a H_2O:NH_3=9:1 mixture at a temperature of 15 K. At the low frequency side of the spectrum the H_2O libration mode (centered around $770 \ cm^{-1}$, or 13 μm) starts showing up for the H_2O-containing mixtures. — (*Right*) Temperature effect on a H_2O:NH_3=9:1 mixture: decreasing FWHM with increasing temperature.
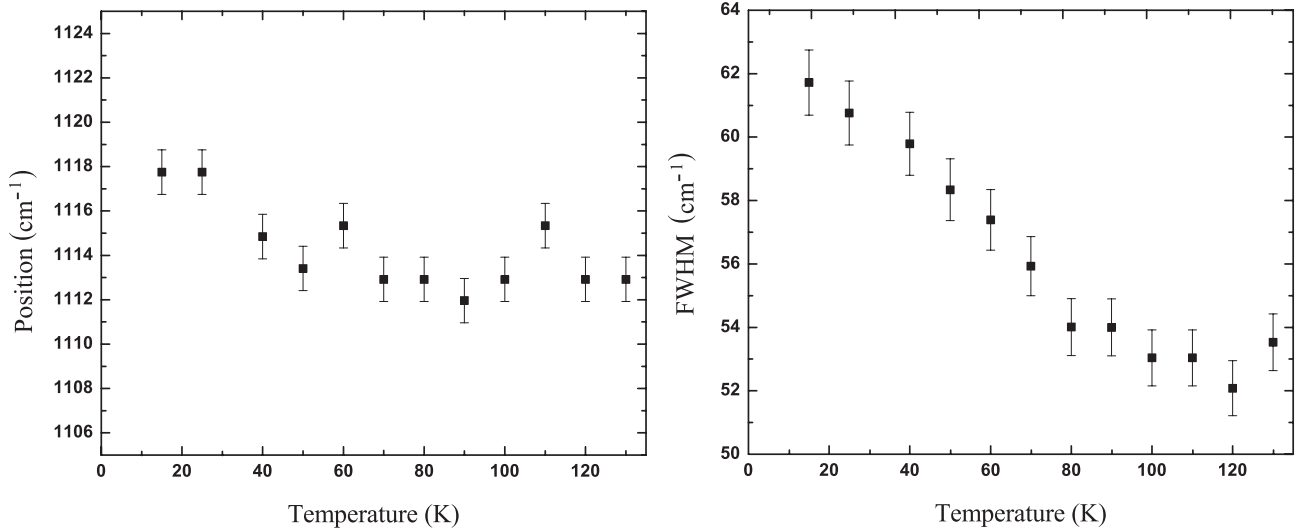

Fig. 7.— A plot indicating the changes in peak position (left) and FWHM (right) of the NH_3 ν_2 umbrella mode as a function of temperature in a 9:1 H_2O:NH_3 ice.
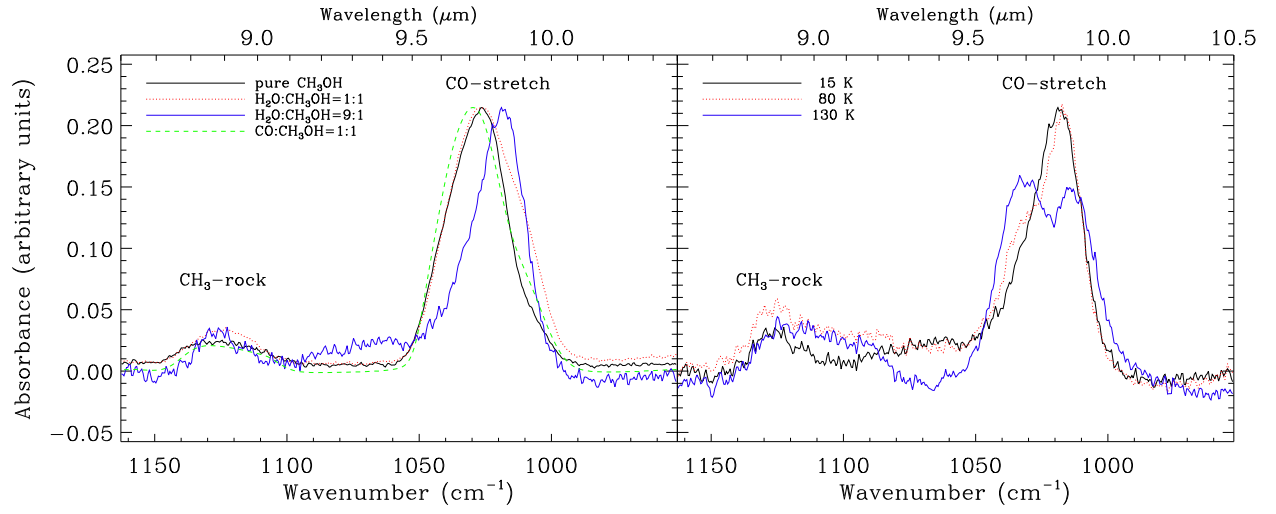
Fig. 8.— (*Left*) Spectra of the CH$_3$OH ν_{CO} modes and ν_{CH3} modes for pure CH$_3$OH, a H$_2$O:CH$_3$OH=1:1, a H$_2$O:CH$_3$OH=9:1 and a CO:CH$_3$OH=1:1 ice mixture at a temperature of 15 K. — (*Right*) Temperature effect on the CO-stretch mode of a H$_2$O:CH$_3$OH=9:1 mixture.

Fig. 9.— Spectra of CH$_3$OH:CO mixtures in the range of the methanol CO stretch mode and the methanol CH$_3$ rock mode. A small blue shift together with a clear substructure are seen upon mixing in more CO.

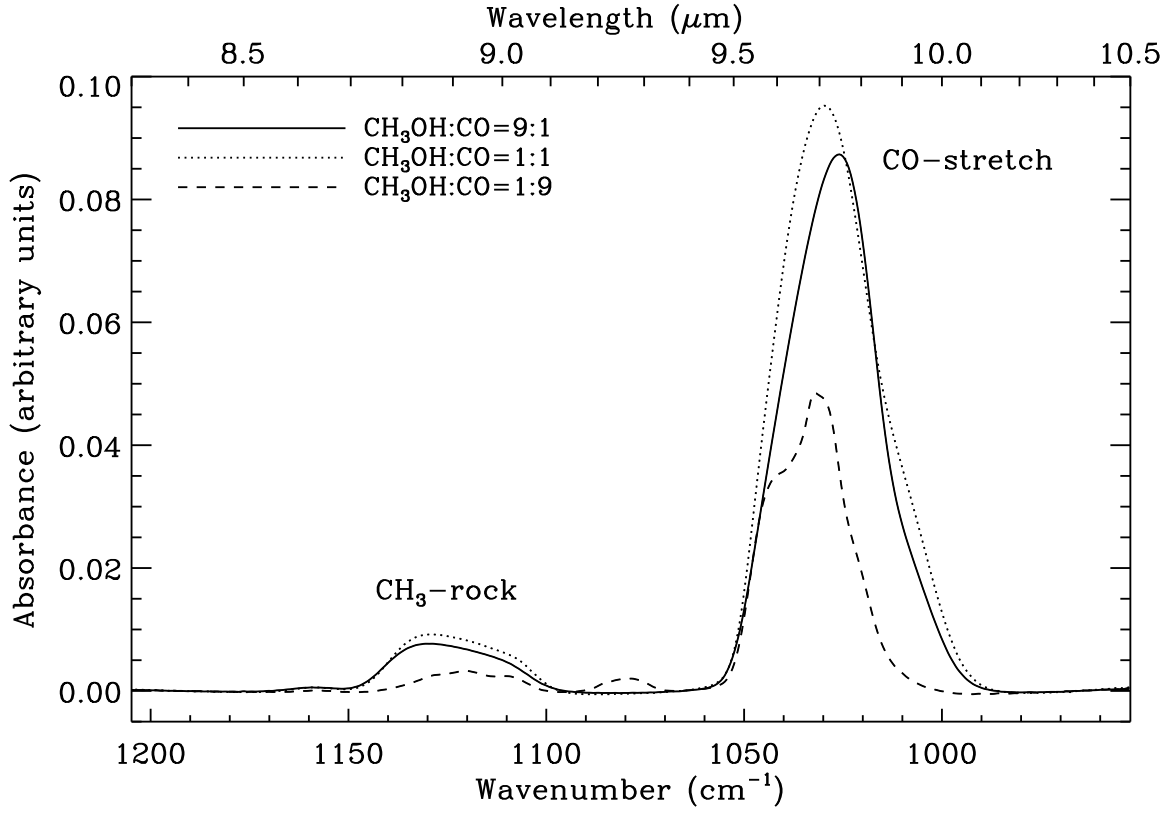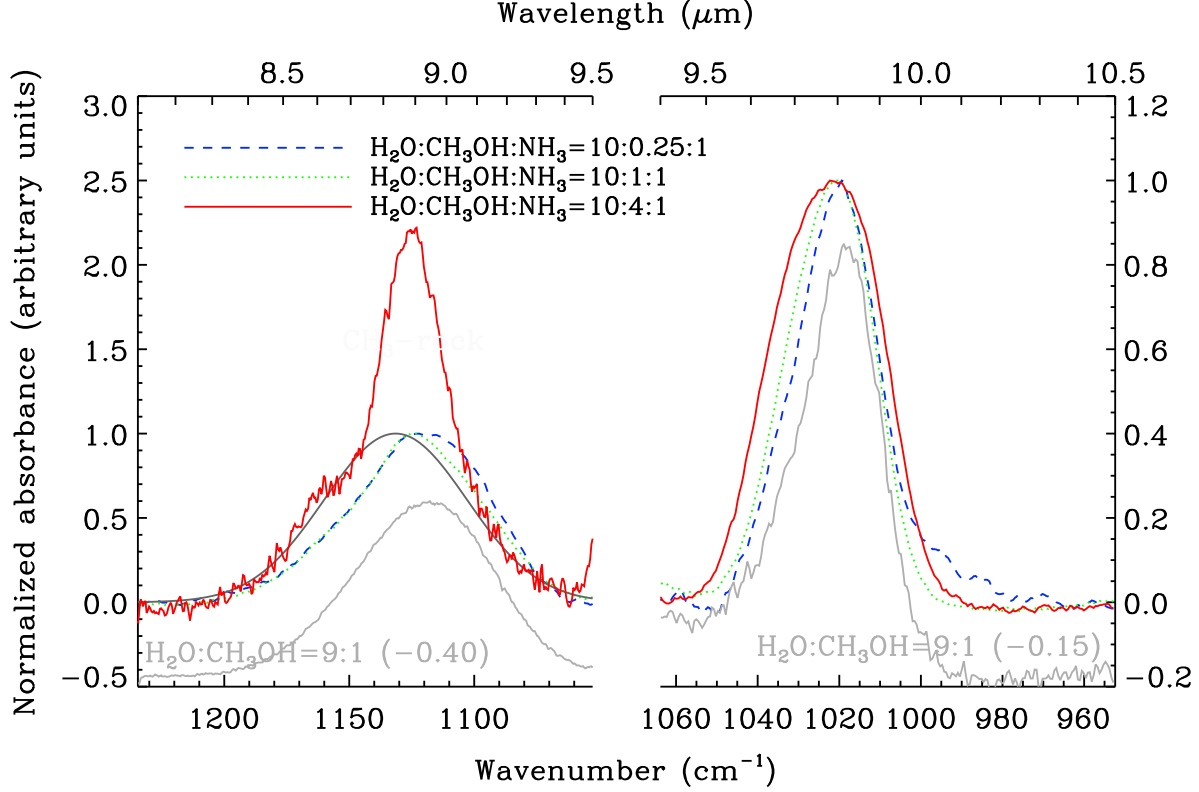Fig. 10.— Normalized spectra of the CH_3OH ν_4 C–O mode (right panel), and NH_3 ν_2 umbrella mode (left panel) for a $H_2O:CH_3OH:NH_3=10:0.25:1$, a $H_2O:CH_3OH:NH_3=10:1:1$ and a $H_2O:CH_3OH:NH_3=10:4:1$ mixture at a temperature of 15 K. These mixture ratios span the range of observed interstellar column density ratios. Spectra were normalized to better show the changes in band maximum position and FWHM of each feature. Spectra of a $H_2O:CH_3OH=9:1$ and a $H_2O:NH_3=1:1$ mixture were offset and overlaid in light grey in the right and left panel, respectively. In the case of $H_2O:CH_3OH:NH_3=10:4:1$, the NH_3 ν_2 umbrella mode is heavily blended with the CH_3OH ν_7 CH_3 rocking mode, so that the dark grey line actually shows the Gaussian fit to the underlying NH_3 feature, whereas the full 9-μm feature is shown in black.

– 31 –

4. Comparison between astronomical and laboratory data

4.1. 8-10 μm range

The FWHM and band positions of the NH_3 and CH_3OH features measured in the laboratory and astronomical spectra are shown in Figs. 11 (for NH_3) and 12 (for CH_3OH). For the YSOs, the values obtained after removal of the silicate absorption (see Section 2) using the local continuum method are indicated by filled squares, whereas those obtained from the template method are plotted with open squares. Note that the presence of significant amounts of CH_3OH may artificially lower the inferred NH_3 ν_2 width in CH_3OH rich sources (indicated with * in Table 2) because of the contribution of the narrower ν_7 CH_3-rock mode.

Regardless of the method used to subtract the continuum, or the type of source (CH_3OH-rich/poor), we find that the observational band positions of the ν_2 NH_3 umbrella mode absorptions vary, within the errors, between 8.9 and 9.1 μm. This position is clearly most consistent with water-rich ice mixtures, and not with pure NH_3 or CO/CO_2 rich ices. The derived *Spitzer* FWHM values range between 0.23 and 0.32 μm (except for B1-b : 0.39 μm), when using the local continuum method, not depending on whether the target is CH_3OH-rich or -poor. For the template method, CH_3OH-rich sources generally tend to have a narrower inferred FWHM, 0.3–0.5 μm, contrary to what would be expected if the NH_3 mode is contaminated by the CH_3-rock feature. In any case, most of these widths are still narrower than the laboratory FWHM values. Thus, Figs. 11 and 12 suggest that the template method for subtraction of the 10 μm silicate absorption is more consistent with the laboratory measurements, but both methods probably miss some weak NH_3 absorption features in the broad line wings where they blend with the continuum at the S/N of the data. If so, the too small line widths inferred from the data would mean that we have underestimated NH_3 abundances by a up to a factor of 2.
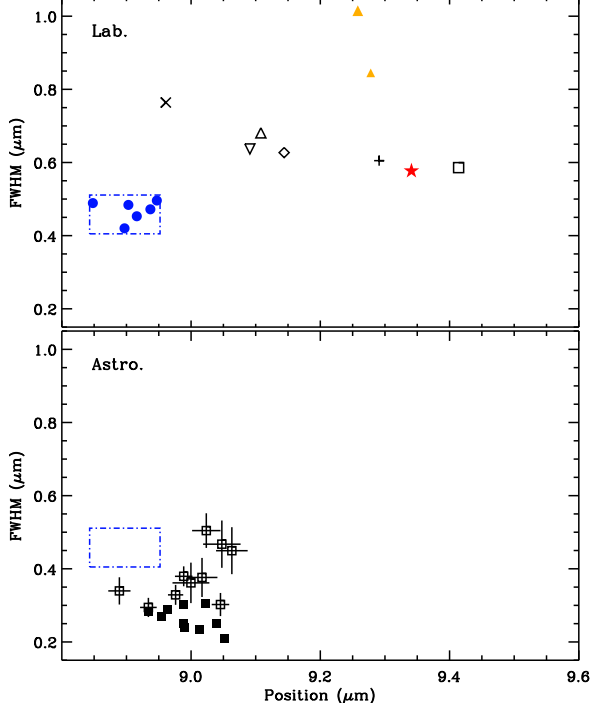
Fig. 11.— FWHM and band maximum position of the NH$_3$ feature measured in the laboratory mixtures at 15 K ("Lab.", top panel) and in the *Spitzer* spectra ("Astro.", bottom panel). In the top panel, the filled star indicates pure NH$_3$, filled circles represent H$_2$O-rich mixtures and filled triangles are for NH$_3$:CH$_3$OH mixtures (an increasing symbol size indicative of increasing CH$_3$OH content). Other symbols are as follows: + for NH$_3$:H$_2$O=1:0.11, $\triangledown$ for NH$_3$:H$_2$O=1:1, $\diamond$ for NH$_3$:H$_2$O:CO=1:1:1, $\triangle$ for NH$_3$:H$_2$O:CO$_2$=1:1:1, $\square$ for NH$_3$:CO:CO$_2$=1:1:1, $\times$ for NH$_3$:CH$_3$OH:H$_2$O=1:1:1. In the bottom panel, open and filled squares indicate values obtained with the template and local continuum method, respectively. The dash-dot polygons delimitate the parameter space of FWHM and positions corresponding to H$_2$O-rich mixtures.
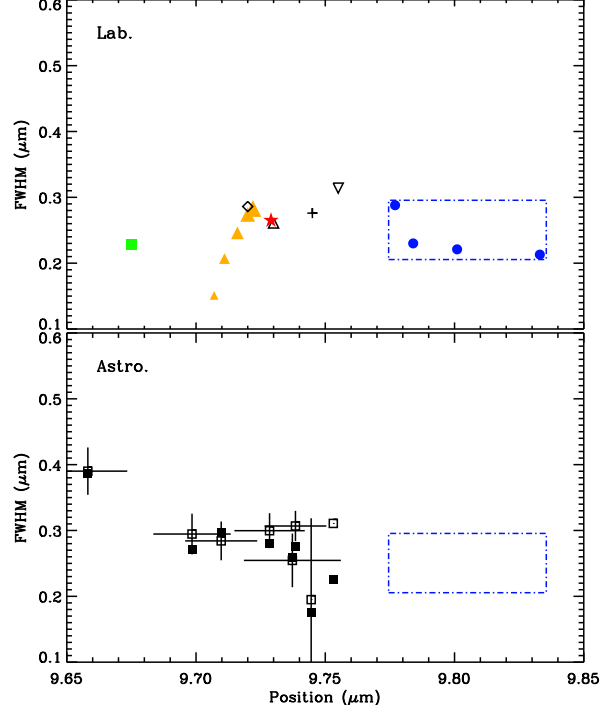
Fig. 12.— Same as Fig. 11 but for CH$_3$OH. In the top panel, the filled star is for pure CH$_3$OH, the filled square is representative of a CO-rich mixture. All other symbols (top and bottom panels) have the same meaning as in Fig. 11, except for the following in the top panel: + for NH$_3$:CH$_3$OH:H$_2$O=1:1:1, $\triangledown$ for CH$_3$OH:H$_2$O=1:1, $\diamond$ for CH$_3$OH:CO=1:1, $\triangle$ for CH$_3$OH:CO=9:1.

The observational band position and FWHM of the CH_3OH features derived with either the local continuum or template method are clustered around 9.7–9.75 μm, with the exception of R CrA IRS 5 at 9.66 μm. Similarly the FWHM of the CH_3OH features are all very similar between $\sim$0.22 and 0.32 μm, except for R CrA IRS 5 with 0.39 μm. These values agree (with a few exceptions) with the values obtained from the laboratory spectra. Note that the observed positions of the CH_3OH feature are all on the low side of the laboratory range. Since the position of this feature shifts to higher wavelengths with increasing water content, the observed low values could therefore indicate that CH_3OH and H_2O are not well mixed and that there exists a separate CH_3OH-rich component, as suggested in previous work (e.g. Pontoppidan et al. 2003; Skinner et al. 1992). Alternatively, the low values could be due to the presence of CO as indicated by the CH_3OH feature shift to 9.70 μm in CH_3OH:CO=1:1. Both interpretations would be consistent with the bulk of the CH_3OH formation coming from hydrogenation of a CO-rich layer, rather than photochemistry in a water-rich matrix. However, the shift from the water-rich mixtures is small, and some water-rich fraction cannot be excluded with the current spectral resolution.

4.2. The 3 and 6 μm ranges

Dartois & d'Hendecourt (2001) discussed the possibility of a 3.47 μm absorption band which could be related to the formation of an ammonia hydrate in the ice mantles: they found that if this band were mostly due to this hydrate, then ammonia abundances would be at most 5% with respect to water ice. Considering the fact that our derived abundances are larger than 10% in some sources, it is necessary to investigate the effect of such a high abundance on the ammonia features in other spectral ranges. For this, depending on the NH_3-to-CH_3OH abundance ratio observed in the *Spitzer* spectra, we scale one of the following laboratory spectra to the 9 μm NH_3 feature: H_2O:NH_3=9:1, H_2O:NH_3=4:1,

$H_2O:CH_3OH:NH_3=10:1:1$, $H_2O:CH_3OH:NH_3=10:4:1$. Figure 13 illustrates the comparison between the *Spitzer* and scaled laboratory spectra for the relevant wavelength ranges for a couple of sources, while Figures C.1-a and -b (see Appendix C) show the comparison for all sources where NH_3 was detected.

For further comparison, we also overplotted in Fig. C.1 the following spectra: (i) the pure H_2O ice spectrum derived from the H_2O column density quoted in Boogert et al. (2008) (deep blue); and (ii) for sources with 3 μm data, the pure H_2O spectrum scaled to the optical depth of the 3-μm feature of the mixed ice laboratory spectrum (purple-dotted). The difference between this scaled pure water spectrum and the mixed ice spectrum gives an indication of the contribution of ammonia features around 3.47 and 6.1 μm.

We then determined the contributions from the NH_3 features to the integrated optical depths of the 3 and 6 μm bands and to the optical depth of component C2, a feature at 6.0-6.4 μm arising from a blend of several species, including NH_3, H_2O, CO_2, $HCOO^-$ (see Paper I for more details). These contributions are reported in Table 3.
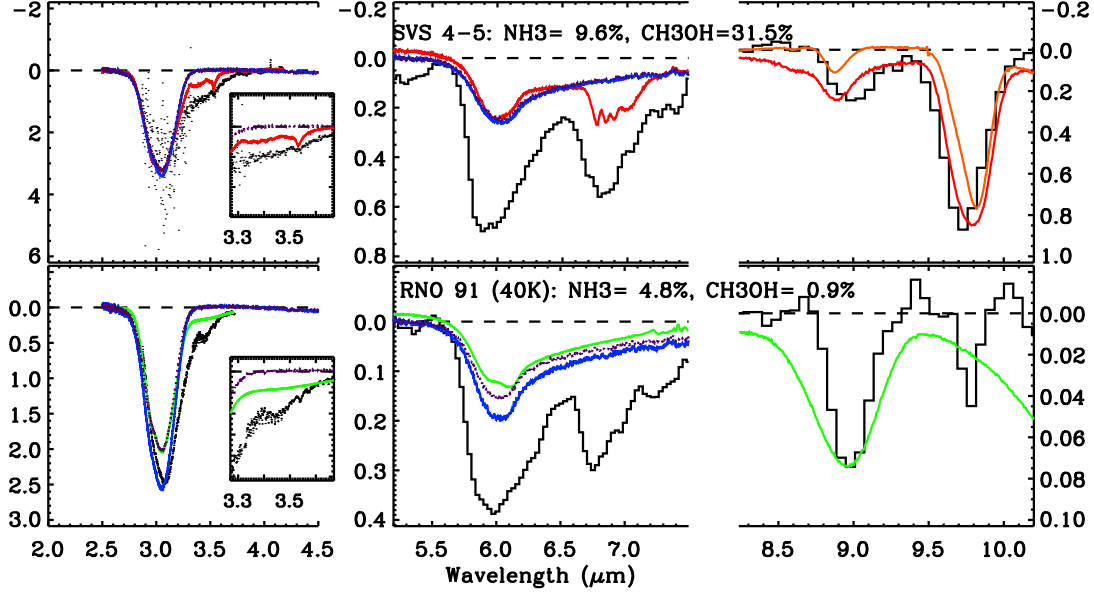
Fig. 13.— Comparison of astronomical data (VLT or Keck measurements at short wavelengths, IRS *Spitzer* observations elsewhere) and laboratory spectra in selected wavelength ranges: 2.0-4.5 μm (left panels), 5.2-7.5 μm (middle panels) and 8.2-10.2 μm (right panels, silicate absorption subtracted via the template method). Overlaid in red and green are laboratory spectra corresponding to $H_2O:CH_3OH:NH_3$=10:4:1 and $H_2O:NH_3$=9:1, respectively, scaled to the 9-μm NH_3 umbrella mode. The dark blue line represents the pure water laboratory spectrum scaled to the water column density taken in paper I. The dotted purple line corresponds to a pure water spectrum scaled to the 3-μm water feature of the mixed ice spectrum, showing the contribution of NH_3 features around 3.47 and 6.1 μm. The laboratory spectra are recorded at 15 K unless indicated differently.

Table 3.   NH$_3$ contribution to the 3 and 6 μm bands

Source	$\dfrac{\int \tau_{H_2O,3.0}}{\int \tau_{3.0}}$	$\dfrac{\int \tau_{mix,3.0}}{\int \tau_{3.0}}$	$\dfrac{\int_{1562}^{1785} \tau_{H_2O}}{\int_{1562}^{1785} \tau}$	$\dfrac{\int_{1562}^{1785} \tau_{mix}}{\int_{1562}^{1785} \tau}$	$\dfrac{\int \tau_{NH_3,6.16}}{\int_{1562}^{1785} \tau_{H_2O}}$	$\dfrac{\tau_{NH_3,6.16}}{\tau_{C2}}$
			Sources with template			
IRAS 03235+3004	–	–	0.50	0.24	0.02	0.61
IRAS 03254+3050	0.73	1.30	0.56	0.92	0.12	1.72
IRAS 04108+2803	0.70	0.67	0.58	0.53	0.06	0.49
HH 300	0.70	0.57	0.50	0.39	0.05	0.45
IRAS 08242-5050	0.76	0.72	0.50	0.45	0.06	0.46
IRAS 08242-5050	0.76	0.56	0.50	0.35	0.05	0.36
2MASSJ17112317-272431	–	–	0.69	0.53	0.05	4.23
SVS 4-5	0.91	0.94	0.42	0.29	0.00	0.08
R CrA IRS 5	0.85	0.42	0.63	0.29	0.03	0.21
			Sources with no associated template			
RNO 15	0.80	1.97	0.53	1.23	0.16	0.45
IRAS 03271+3013	–	–	0.36	0.44	0.05	0.60
B1-a	–	–	0.67	0.43	0.03	0.57
L1489 IRS	0.78	0.88	0.60	0.56	0.04	0.83
RNO 91	0.94	0.94	0.53	0.45	0.04	0.53
IRAS 17081-2721	0.65	0.95	0.62	0.75	0.05	1.64
EC 74	0.95	2.34	0.57	1.18	0.09	0.76
EC 92	0.90	0.35	0.38	0.10	0.00	0.01
CrA IRS7 B	–	–	0.81	0.19	0.00	0.08
L1014 IRS	–	–	0.62	0.55	0.06	0.34

Note. — A dash indicates that the ratio was not calculated due to the high noise in the 3-μm spectrum.

Parameters are:

$\int \tau_{H_2O,3.0}$ = integrated optical depth of pure water at 3 μm, determined from the column density of paper I and a band strength of 2.0×10^{-16} cm^{-1}.

$\int \tau_{3.0}$, $\int \tau_{mix,3.0}$ = integrated optical depth over the entire 3 μm region for, respectively, the considered source and the corresponding laboratory mixture (selected from the NH$_3$ feature at 9 μm).

$\int_{1562}^{1785} \tau_{H_2O}$, $\int_{1562}^{1785} \tau$, $\int_{1562}^{1785} \tau_{mix}$ = integrated optical depth of, respectively, pure water, source spectrum, and laboratory mixture, between 1562 and 1785 cm^{-1} (5.6 to 6.4 μm).

$\int \tau_{\mathrm{NH_3},6.16}$, $\tau_{\mathrm{NH_3},6.16}$ = integrated and peak optical depth of the 6.16 μm feature of ammonia obtained after subtraction of a pure water spectrum scaled to the optical depth at 3 μm of the laboratory mixture.

τ_{C2} = peak optical depth of the C2 component from paper I.

Figure C.1 and Table 3 show that (i) the scaled laboratory spectra generally do not overestimate the observed absorption features, and (ii) for most sources, the presence of NH_3 at the level we determine from the 9 μm feature does not explain by itself the depth of the C2 component and of the red wing of the 3 μm band. Hence, our inferred NH_3 abundances up to 15% from the 9.7 μm data are not in conflict with the lack of other NH_3 features. The only exceptions are two sources (RNO 15 and EC 74), for which the scaled mixed ice spectrum exceeds the data in the 3-μm range. In the case of RNO 15, the NH_3 abundance could have been overestimated due to the contribution of the CH_3OH CH_3-rock feature at $\sim 9\mu$m. For EC 74, this overestimate and the presence of emission weakens the identification of the NH_3 signature. In both cases, the quoted NH_3 abundances should be considered as upper limits.

Overall, our reported NH_3 abundances are up to a factor of three larger than the upper limits derived by Dartois & d'Hendecourt (2001). Firstly, let's recall that the conclusions in their study and in ours are drawn from the analysis of different samples. Secondly, Dartois & d'Hendecourt made an assumption that does not apply to our sample: indeed, they considered a grain size distribution including also scattering from larger grains, producing an enhanced 3-μm wing, whereas the results presented here can be taken as representative of NH_3 absorption from small grains. It is beyond the scope of this paper to investigate the effects of grain size distribution and scattering in as much detail as did Dartois & d'Hendecourt (2001).

4.3. Nitrogen ice inventory

The confirmation of the presence of relatively large amounts of solid NH_3, up to 15%, in interstellar ices solves a long-standing problem. Indeed, the detection of solid NH_3 has remained elusive and/or controversial, despite a number of clues suggesting its presence:

- High cosmic abundance of atomic nitrogen : $N_N/N_H = 7.76 \times 10^{-5}$ (Savage & Sembach 1996), only a factor of a few below those of oxygen and carbon. Here N_H indicates the total number of hydrogen nuclei, $N_H = N(H) + 2N(H_2)$.

- High abundances of gaseous NH_3 of $N_{NH_3}/N_{H_2} \sim 10^{-6} - 10^{-5}$ in the Orion-KL nebula (Barrett et al. 1977; Genzel et al. 1982) and in other hot cores such as G9.62+0.19, G29.96−0.02, G31.41+0.31 (Cesaroni et al. 1994), and G10.47+0.03 (Cesaroni et al. 1994; Osorio et al. 2009).

- Identification of substantial amounts of OCN^- (e.g. van Broekhuizen et al. 2004, 2005) and NH_4^+ in ices (e.g. Schutte & Khanna 2003; Boogert et al. 2008): considering that these ions form via reactions involving NH_3, the non-detection of solid NH_3 would be puzzling.

Our results can be used to draw up a possible nitrogen budget. Assuming $N_{H_2O}/N_H \sim 5 \times 10^{-5}$ (Pontoppidan et al. 2004; Boogert et al. 2004), and average abundances w.r.t. H_2O of 5.5% for NH_3 (see §2.3), 7% for NH_4^+ (from Table 3 of Paper I), and 0.6% for OCN^- (van Broekhuizen et al. 2005), then the NH_3, NH_4^+ and OCN^- abundances with respect to total H are 2.8, 3.5, and 0.3 $\times10^{-6}$ respectively. This corresponds to, respectively, 3.4, 4.4 and 0.4% of the atomic nitrogen cosmic abundance so that, in total, about 10% of the cosmically available nitrogen would be locked up in ices, leaving solid and gaseous N_2, N and HCN as other substantial nitrogen carriers. The main uncertainty in this determination is the adopted H_2O ice abundance with respect to total H; in several sources this may well be a factor of 2 larger, leading to about 20% of the nitrogen accounted for in ices.

5. Conclusion

We have analyzed in detail the 8-10 μm range of the spectra of 41 low-mass YSOs obtained with *Spitzer* and presented in Boogert et al. (2008). The sources are categorized into three types: straight, curved and rising 8 μm silicate wings, and for each category template sources with little or no absorption from ices around 9-10 μm have been determined. This has led to two ways of subtracting the contribution from the 10 μm silicate absorption: first, by determining a local continuum, and second, by scaling the templates to the optical depth at 9.7 μm. The two methods give consistent band positions of the NH_3 features, but the resulting widths can be up to a factor of two larger using the template continuum method. NH_3 ice is definitely detected in 24 of the 41 sources with abundances of $\sim$2 to 15 % w.r.t. H_2O, with an average abundance of 5.5$\pm$2.0 %. These abundances have estimated uncertainties up to a factor of two and are consistent with other features in the 3 and 6 μm ranges. CH_3OH is often detected as well, but the NH_3/CH_3OH abundance ratio changes strongly from source to source. Our inferred CH_3OH column densities are consistent with the values derived in paper I.

Targeted laboratory experiments have been carried out to characterize the NH_3 and CH_3OH profiles (position, FWHM, integrated absorbance). Comparison with the observational data shows reasonable agreement for the position of the NH_3 feature in H_2O-rich ices, but the observed widths are systematically smaller than the laboratory ones for nearly all sources. The silicate template continuum method gives widths that come closest to the laboratory values. This difference in width (i.e. widths derived from astronomical spectra smaller than those in the laboratory spectra) suggests that the NH_3 abundances determined here may be on the low side.

The CH_3OH profile is most consistent with a significant fraction of the CH_3OH in a relatively pure or CO-rich phase, consistent with its formation by the hydrogenation of CO

ice. In contrast, the most likely formation route of NH$_3$ ice remains hydrogenation of atomic N together with water ice formation in a relatively low density molecular phase. Finally, the nitrogen budget indicates that up to 10 to 20 % of nitrogen is locked up in known ices.

A. Parameters of Gaussian fits

Table A.1.   Parameters of Gaussian fits to the NH_3 feature.

Source	NH₃, local			NH₃, template		
	λ (μm)	FWHM (μm)	τ_{peak}	λ (μm)	FWHM (μm)	τ_{peak}
IRAS 03235+3004	8.93±0.02	0.28±0.03	0.23±0.02	8.93±0.01	0.29±0.03	0.30±0.02
L1455 IRS3	8.99±0.03	0.24±0.07	0.02±0.01	9.02±0.02	0.38±0.05	0.04±0.01
IRAS 03254+3050	9.04±0.01	0.25±0.03	0.10±0.01	8.99±0.01	0.38±0.03	0.12±0.01
B1-b*	9.05±0.03	0.39±0.06	0.25±0.02	9.07±0.03	0.40±0.06	0.31±0.03
IRAS 04108+2803	8.99±0.02	0.25±0.04	0.05±0.01	9.05±0.03	0.47±0.06	0.04±0.01
HH 300	9.01±0.02	0.23±0.05	0.04±0.01	9.06±0.02	0.45±0.06	0.05±0.01
IRAS 08242-5050	9.02±0.01	0.31±0.03	0.15±0.01	9.05±0.01	0.30±0.03	0.15±0.01
IRAS 15398-3359	8.96±0.01	0.29±0.03	0.30±0.02	8.98±0.01	0.33±0.03	0.41±0.02
B59 YSO5	8.95±0.01	0.27±0.03	0.18±0.02	8.89±0.02	0.34±0.04	0.18±0.02
2MASSJ17112317-272431	8.99±0.01	0.30±0.02	0.43±0.02	9.02±0.02	0.50±0.05	0.41±0.04
SVS 4-5*	9.00±0.01	0.26±0.03	0.16±0.02	9.01±0.01	0.30±0.03	0.26±0.02
R CrA IRS 5	9.05±0.02	0.21±0.04	0.04±0.01	9.00±0.03	0.36±0.06	0.04±0.01
RNO 15	9.05±0.02	0.20±0.04	0.04±0.01	–	–	–
IRAS 03271+3013	8.96±0.02	0.25±0.04	0.20±0.02	–	–	–
B1-a	8.98±0.02	0.25±0.04	0.14±0.02	–	–	–
L1489 IRS	9.02±0.01	0.27±0.03	0.09±0.01	–	–	–
IRAS 13546-3941	8.99±0.02	0.27±0.03	0.03±0.00	–	–	–
RNO 91	8.98±0.01	0.26±0.03	0.08±0.01	–	–	–
IRAS 17081-2721	8.97±0.02	0.24±0.04	0.04±0.00	–	–	–
EC 74	9.01±0.02	0.22±0.05	0.05±0.01	–	–	–
EC 82	8.94±0.01	0.29±0.03	0.04±0.00	–	–	–
EC 90	8.95±0.02	0.18±0.05	0.04±0.01	–	–	–
EC 92*	8.99±0.02	0.25±0.05	0.03±0.00	–	–	–
CK4	8.99±0.02	0.32±0.04	0.03±0.00	–	–	–
CrA IRS7 B*	9.04±0.01	0.26±0.03	0.15±0.01	–	–	–
L1014 IRS	9.03±0.02	0.25±0.05	0.15±0.02	–	–	–

Note. — Uncertainties are statistical errors from the Gaussian fits.

*Sources with $\tau_{9.7\mu m} > 2 \times \tau_{9.0\mu m}$, for which the contribution from the CH_3OH CH_3-rock mode is significant. Since the latter and the NH_3 umbrella mode were difficult to disentangle, a single fit was performed (the reported parameters)

and the integrated optical depth of the ammonia feature was then obtained from the total integrated optical depth at 9 μmby subtracting the estimated contribution of the CH_3OH CH_3-rock mode (see §2.2).

Table A.2. Parameters of Gaussian fits to the CH$_3$OH C-O stretch mode (after subtraction of the continuum with the local and/or template method), and CH$_3$OH column densities (or 3-σ upper limits).

Source	Local continuum				Template continuum				Paper I
	λ (μm)	FWHM (μm)	τ_{peak}	X (% H$_2$O)	λ (μm)	FWHM (μm)	τ_{peak}	X (% H$_2$O)	X (% H$_2$O)
IRAS 03235+3004	9.74±0.02	0.26±0.03	0.35±0.04	4.40±1.04	9.74±0.02	0.25±0.04	0.31±0.04	3.84±0.99	4.20±1.20
L1455 IRS3	9.78±0.01	0.14±0.03	0.03±0.01	3.67±1.80	9.78±0.02	0.26±0.04	0.04±0.01	7.71±3.46	<12.5
IRAS 03254+3050	...	...	...	< 5.4	...	...	...	< 5.4	< 4.6
B1-b	9.71±0.01	0.30±0.03	1.19±0.11	14.15±3.16	9.71±0.01	0.28±0.03	1.21±0.11	13.75±3.12	11.20±0.70
IRAS 04108+2803	...	...	...	< 2.7	9.75±0.00	0.06±0.04	0.04±0.03	0.58±0.62	< 3.5
HH 300	...	...	...	< 4.7	9.74±0.00	0.19±0.12	0.01±0.01	0.78±0.52	< 6.7
IRAS 08242-5050	9.70±0.01	0.27±0.03	0.25±0.02	6.12±1.01	9.70±0.01	0.29±0.03	0.24±0.02	6.39±1.09	5.50±0.30
IRAS 15398-3359	9.73±0.01	0.28±0.03	0.77±0.06	10.26±3.02	9.73±0.01	0.30±0.03	0.75±0.06	10.69±3.14	10.30±0.80
B59 YSO5	...	...	...	< 1.2	...	...	...	< 1.2	< 1.3
2MASSJ17112317-272431	9.75±0.02	0.23±0.04	0.13±0.02	1.03±0.22	...	...	...	< 2.0	< 3.2
SVS 4-5	9.74±0.01	0.28±0.03	0.77±0.06	26.38±6.17	9.74±0.01	0.31±0.02	0.83±0.06	31.50±7.12	25.20±3.50
R CrA IRS 5	9.66±0.01	0.39±0.03	0.07±0.00	5.68±0.60	9.66±0.02	0.39±0.04	0.07±0.00	5.51±0.72	6.60±1.60
RNO 15	9.65±0.03	0.44±0.07	0.02±0.00	11.13±2.16	...	...	...	...	< 5.0
IRAS 03271+3013	...	...	...	< 4.3	...	...	...	...	< 5.6
B1-a	...	...	...	< 2.4	...	...	...	...	< 1.9
L1489 IRS	9.78±0.02	0.10±0.03	0.03±0.01	0.44±0.22	...	...	...	...	4.90±1.50
IRAS 13546-3941	...	...	...	< 2.0	...	...	...	...	< 3.9
RNO 91	9.77±0.01	0.11±0.03	0.05±0.01	0.87±0.32	...	...	...	...	< 5.6
IRAS 17081-2721	...	...	...	< 6.6	...	...	...	...	3.30±0.80
EC 74	...	...	...	<13.5	...	...	...	...	< 9.3
EC 82	...	...	...	<24.6	...	...	...	...	<14.2
EC 90	9.70±0.01	0.32±0.03	0.05±0.00	6.91±0.99	...	...	...	...	6.80±1.60

Table A.2—Continued

Source	Local continuum				Template continuum				Paper I
	λ	FWHM	τ_{peak}	X	λ	FWHM	τ_{peak}	X	X
	(μm)	(μm)		(% H_2O)	(μm)	(μm)		(% H_2O)	(% H_2O)
EC 92	9.73±0.01	0.30±0.02	0.09±0.01	11.16±1.46	$\cdots$	$\cdots$	$\cdots$	$\cdots$	11.70±3.50
CK4	$\cdots$	$\cdots$	$\cdots$	$\cdots$	$\cdots$	$\cdots$	$\cdots$	$\cdots$	$\cdots$
CrA IRS7 B	9.70±0.01	0.33±0.02	0.36±0.02	7.74±1.56	$\cdots$	$\cdots$	$\cdots$	$\cdots$	6.80±0.30
L1014 IRS	9.69±0.03	0.38±0.08	0.10±0.01	3.61±0.99	$\cdots$	$\cdots$	$\cdots$	$\cdots$	3.10±0.80

Note. — This table shows that CH_3OH column densities obtained in this paper are consistent with those in Paper I, which are our recommended values.

Note. — Uncertainties are statistical errors from the Gaussian fits.

B. Additional information on laboratory data

Table B.3.   Ice composition, band maximum position ("peak position"), FWHM and band strength relative to the pure ice ($A_{\rm rel.}$), listed for a set of ice mixtures under investigation.

Ice mixture					Molecule	Peak position		FWHM		$A_{\rm rel.}$		Mode
NH_3	CH_3OH	H_2O	CO	CO_2		cm^{-1}	μm	cm^{-1}	μm			
1	0	0	0	0	NH_3	1070	9.341	66	0.577	1	ν_2	umbrella
1	0	0.11	0	0	NH_3	1076	9.291	70	0.605	1	ν_2	umbrella
1	0	1	0	0	NH_3	1100	9.091	77	0.637	1	ν_2	umbrella
1	0	9	0	0	NH_3	1118	8.947	62	0.496	0.7	ν_2	umbrella
1	0	10	1	0	NH_3	1124	8.897	53	0.420	0.7	ν_2	umbrella
1	0	1	1	0	NH_3	1094	9.144	75	0.627	1	ν_2	umbrella
1	0	10	0	2	NH_3	1122	8.916	57	0.453	0.8	ν_2	umbrella
1	0	1	0	1	NH_3	1098	9.108	82	0.681	0.9	ν_2	umbrella
1	0	0	1	1	NH_3	1062	9.414	66	0.586	0.8	ν_2	umbrella
1	4	0	0	0	NH_3	1129^a	8.856^a	108^a	0.849	0.4^a	ν_2	umbrella
1	4	0	0	0	CH_3OH	1029	9.722	30	0.283	–	ν_4	C-O stretch
1	4	0	0	0	CH_3OH	1128	9.707	35	0.275	–	ν_7	CH_3 rock
1	4	0	0	0	CH_3OH	2823	3.543	28	0.035	–	ν_2	C-H stretch
1	2	0	0	0	NH_3	1111^a	8.994^a	115^a	0.934	0.6^a	ν_2	umbrella
1	2	0	0	0	CH_3OH	1029	9.720	29	0.274	–	ν_4	C-O stretch
1	2	0	0	0	CH_3OH	1132	8.833	35	0.273	–	ν_7	CH_3 rock
1	2	0	0	0	CH_3OH	2820	3.546	26	0.033	–	ν_2	C-H stretch
1	1	0	0	0	NH_3	1086	9.209	137	1.166	0.8	ν_2	umbrella
1	1	0	0	0	CH_3OH	1029	9.716	26	0.246	–	ν_4	C-O stretch
1	1	0	0	0	CH_3OH	1135	8.813	44	0.342	–	ν_7	CH_3 rock
1	1	0	0	0	CH_3OH	2817	3.550	26	0.033	–	ν_2	C-H stretch
1	0.5	0	0	0	NH_3	1080	9.258	118	1.015	0.8	ν_2	umbrella
1	0.5	0	0	0	CH_3OH	1030	9.711	22	0.207	–	ν_4	C-O stretch
1	0.5	0	0	0	CH_3OH	1128^a	8.865^a	35^a	0.275	–	ν_7	CH_3 rock
1	0.5	0	0	0	CH_3OH	2813	3.555	27	0.034	–	ν_2	C-H stretch
1	0.25	0	0	0	NH_3	1078	9.278	98	0.845	0.9	ν_2	umbrella
1	0.25	0	0	0	CH_3OH	1030	9.707	16	0.151	–	ν_4	C-O stretch
1	0.25	0	0	0	CH_3OH	$–^a$	$–^a$	$–^a$	$–^a$	–	ν_7	CH_3 rock
1	0.25	0	0	0	CH_3OH	2808^a	3.561^a	17^a	0.022	$–^a$	ν_2	C-H stretch
1	1	1	0	0	NH_3	1116^a	8.961	95	0.764	0.7	ν_2	umbrella
1	1	1	0	0	CH_3OH	1026	9.745	29	0.276	–	ν_4	C-O stretch

Table B.3—Continued

Ice mixture					Molecule	Peak position		FWHM		$A_{\rm rel.}$		Mode
NH_3	CH_3OH	H_2O	CO	CO_2		cm^{-1}	μm	cm^{-1}	μm			
1	1	1	0	0	CH_3OH	1125^a	8.888^a	32^a	0.253	–	ν_7	CH_3 rock
1	1	1	0	0	CH_3OH	2824	3.541	26	0.033	–	ν_2	C-H stretch
1	0.25	10	0	0	NH_3	1119	8.937	59	0.472	1	ν_2	umbrella
1	0.25	10	0	0	CH_3OH	1017	9.833	22	0.213	–	ν_4	C-O stretch
1	0.25	10	0	0	CH_3OH	$-^a$	$-^a$	$-^a$	$-^a$	–	ν_7	CH_3 rock
1	0.25	10	0	0	CH_3OH	2829^a	3.534^a	30^a	0.037	–	ν_2	C-H stretch
1	1	10	0	0	NH_3	1123	8.903	61	0.484	1	ν_2	umbrella
1	1	10	0	0	CH_3OH	1022	9.784	24	0.230	–	ν_4	C-O stretch
1	1	10	0	0	CH_3OH	$-^a$	$-^a$	$-^a$	$-^a$	–	ν_7	CH_3 rock
1	1	10	0	0	CH_3OH	2830	3.533	15	0.019	–	ν_2	C-H stretch
1	4	10	0	0	NH_3	1130	8.848	62	0.489	–	ν_2	umbrella
1	4	10	0	0	CH_3OH	1023	9.777	30	0.288	–	ν_4	C-O stretch
1	4	10	0	0	CH_3OH	1124	8.896	23	0.183	–	ν_7	CH_3 rock
1	4	10	0	0	CH_3OH	2830	3.534	14	0.017	–	ν_2	C-H stretch
0	1	0	0	0	CH_3OH	1028	9.729	28	0.265	1	ν_4	C-O stretch
0	1	0	0	0	CH_3OH	1125	8.888	34	0.269	1	ν_7	CH_3 rock
0	1	0	0	0	CH_3OH	2828	3.536	33	0.041	1	ν_2	C-H stretch
0	1	1	0	0	CH_3OH	1025	9.755	33	0.314	–	ν_4	C-O stretch
0	1	1	0	0	CH_3OH	1124	8.897	40	0.317	–	ν_7	CH_3 rock
0	1	1	0	0	CH_3OH	2828	3.536	23	0.029	–	ν_2	C-H stretch
0	1	9	0	0	CH_3OH	1020	9.801	23	0.221	–	ν_4	C-O stretch
0	1	9	0	0	CH_3OH	1126	8.883	13	0.103	–	ν_7	CH_3 rock
0	1	9	0	0	CH_3OH	2828	3.536	23	0.029	–	ν_2	C-H stretch
0	1	0	9	0	CH_3OH	1034	9.675	25	0.229	–	ν_4	C-O stretch
0	1	0	9	0	CH_3OH	1119	8.938	30	0.242	–	ν_7	CH_3 rock
0	1	0	9	0	CH_3OH	2831	3.532	–	–	–	ν_2	C-H stretch
0	1	0	9	0	CO	2138	4.677	7	0.014	–	ν_1	C-O stretch
0	1	0	1	0	CH_3OH	1029	9.720	30	0.286	–	ν_4	C-O stretch
0	1	0	1	0	CH_3OH	1124	8.898	32	0.258	–	ν_7	CH_3 rock
0	1	0	1	0	CH_3OH	2830	3.534	–	–	–	ν_2	C-H stretch
0	1	0	1	0	CO	2136	4.682	9	0.020	–	ν_1	C-O stretch

Table B.3—Continued

Ice mixture					Molecule	Peak position		FWHM		$A_{\rm rel.}$		Mode
NH_3	CH_3OH	H_2O	CO	CO_2		cm^{-1}	μm	cm^{-1}	μm			
0	9	0	1	0	CH_3OH	1028	9.730	28	0.261	–	ν_4	C-O stretch
0	9	0	1	0	CH_3OH	1125	8.890	32	0.255	–	ν_7	CH_3 rock
0	9	0	1	0	CH_3OH	2824	3.541	–	–	–	ν_2	C-H stretch
0	9	0	1	0	CO	2135	4.685	9	0.021	–	ν_1	C-O stretch

[a]Band is weak and spectral overlap prohibits accurate fitting.

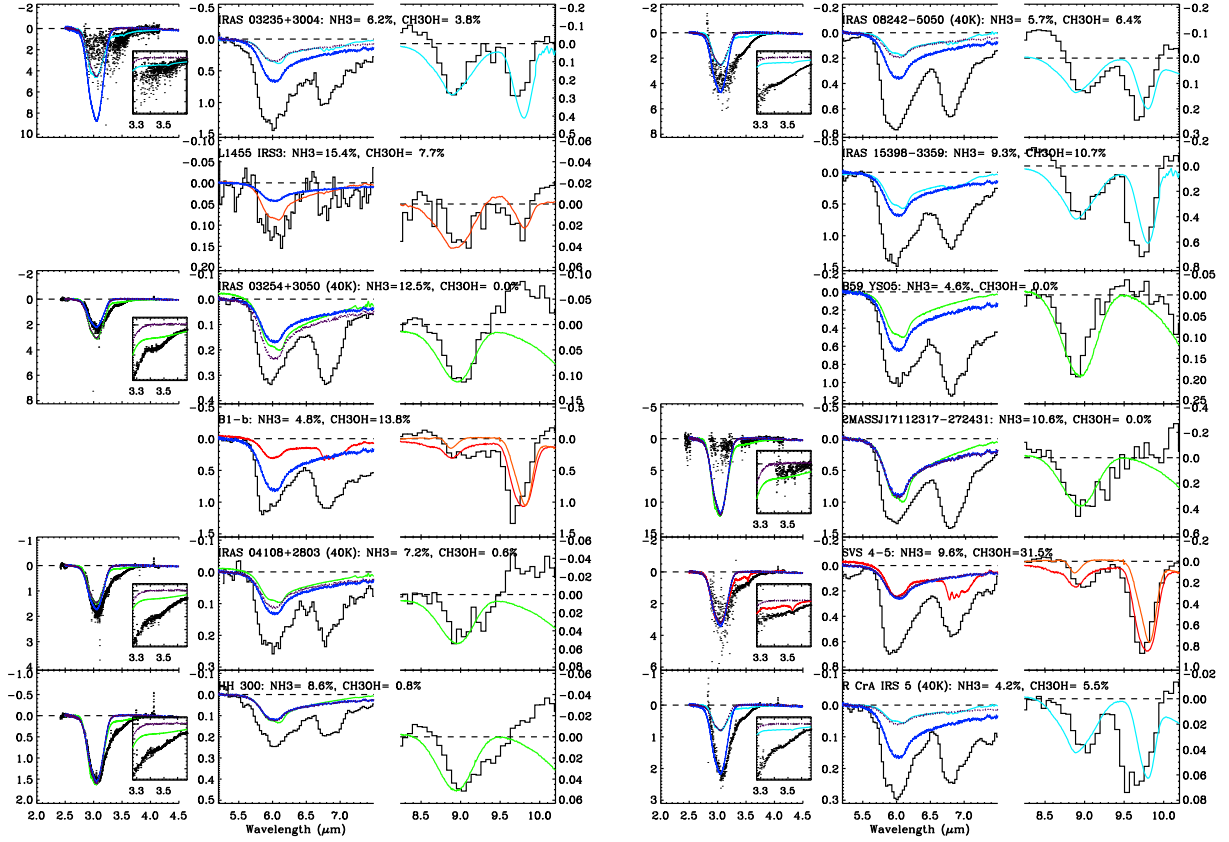C.   Comparison between astronomical and laboratory data for all sources

Fig. C.1.— (a) Comparison between astronomical and laboratory data for sources whose silicate absorption feature was fitted with a template. For a given source (displayed in either the left or right column of the figure), the middle and right panels show 5.2-7.5 and 8.2-10.2 μm regions from IRS *Spitzer* spectra overlaid with laboratory spectra, scaled to the 9-μm NH_3 umbrella mode. The dark blue line represents the pure water laboratory spectrum scaled to the water column density taken in paper I. Other colors are representative of laboratory spectra obtained for the following mixtures: $H_2O:NH_3=9:1$ (green), $H_2O:CH_3OH:NH_3=10:0.25:1$ (orange), $H_2O:CH_3OH:NH_3=10:1:1$ (cyan), and $H_2O:CH_3OH:NH_3=10:4:1$ (red). When available (see Boogert et al. 2008), VLT or Keck data (2.0-4.5 μm, left panel) are also plotted. In this case, we overplotted (dotted purple line) a pure water spectrum scaled to the 3-μm water feature of the mixed ice spectrum. The laboratory spectra are recorded at 15 K unless indicated differently.
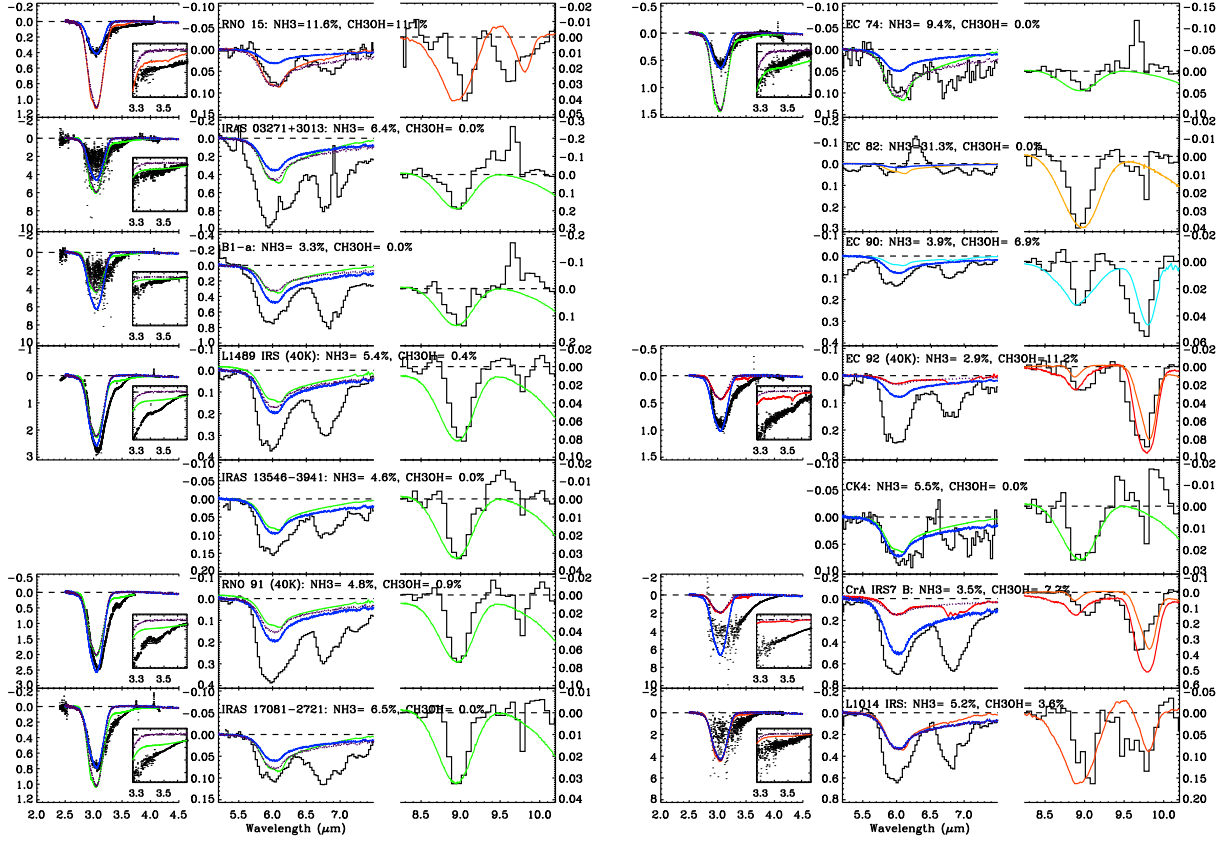
Fig. C.1.— (b) As (a) but for sources with no associated template, i.e. with the 10-μm silicate feature subtracted via the local continuum method. Additionally, yellow represents H_2O:NH_3=4:1 (H. Frazer, priv. comm.).

REFERENCES

Barrett, A. H., Ho, P. T. P., & Myers, P. C. 1977, ApJ, 211, L39

Bernstein, M. P., Dworkin, J. P., Sandford, S. A., Cooper, G. W., & Allamandola, L. J. 2002, Nature, 416, 401

Bisschop, S. E., Fuchs, G. W., Boogert, A. C. A., van Dishoeck, E. F., & Linnartz, H. 2007, A&A, 470, 749

Blake, D., Allamandola, L., Sandford, S., Hudgins, D., & Freund, F. 1991, Science, 254, 548

Blake, G. A., Sutton, E. C., Masson, C. R., & Phillips, T. G. 1987, ApJ, 315, 621

Boogert, A. C. A., Pontoppidan, K. M., Knez, C., Lahuis, F., Kessler-Silacci, J., van Dishoeck, E. F., Blake, G. A., Augereau, J.-C., Bisschop, S. E., Bottinelli, S., Brooke, T. Y., Brown, J., Crapsi, A., Evans, II, N. J., Fraser, H. J., Geers, V., Huard, T. L., Jørgensen, J. K., Öberg, K. I., Allen, L. E., Harvey, P. M., Koerner, D. W., Mundy, L. G., Padgett, D. L., Sargent, A. I., & Stapelfeldt, K. R. 2008, ApJ, 678, 985

Boogert, A. C. A., Pontoppidan, K. M., Lahuis, F., Jørgensen, J. K., Augereau, J.-C., Blake, G. A., Brooke, T. Y., Brown, J., Dullemond, C. P., Evans, N. J., Geers, V., Hogerheijde, M. R., Kessler-Silacci, J., Knez, C., Morris, P., Noriega-Crespo, A., Schöier, F. L., van Dishoeck, E. F., Allen, L. E., Harvey, P. M., Koerner, D. W., Mundy, L. G., Myers, P. C., Padgett, D. L., Sargent, A. I., & Stapelfeldt, K. R. 2004, ApJS, 154, 359

Bouwman, J., Ludwig, W., Awad, Z., Ã-Berg, K. I., Fuchs, G. W., van Dishoeck, E. F., & Linnartz, H. 2007, A&A, 476, 995

Cesaroni, R., Churchwell, E., Hofner, P., Walmsley, C. M., & Kurtz, S. 1994, A&A, 288, 903

Cuppen, H. M., van Dishoeck, E. F., Herbst, E., & Tielens, A. G. G. M. 2009, A&A, submitted

Dartois, E. & d'Hendecourt, L. 2001, A&A, 365, 144

Dartois, E., d'Hendecourt, L., Thi, W., Pontoppidan, K. M., & van Dishoeck, E. F. 2002, A&A, 394, 1057

Dartois, E., Schutte, W., Geballe, T. R., Demyk, K., Ehrenfreund, P., & D'Hendecourt, L. 1999, A&A, 342, L32

d'Hendecourt, L. B. & Allamandola, L. J. 1986, A&AS, 64, 453

Evans, II, N. J., Allen, L. E., Blake, G. A., Boogert, A. C. A., Bourke, T., Harvey, P. M., Kessler, J. E., Koerner, D. W., Lee, C. W., Mundy, L. G., Myers, P. C., Padgett, D. L., Pontoppidan, K., Sargent, A. I., Stapelfeldt, K. R., van Dishoeck, E. F., Young, C. H., & Young, K. E. 2003, PASP, 115, 965

Federman, S. R., Huntress, Jr., W. T., & Prasad, S. S. 1990, ApJ, 354, 504

Fuchs, G. W., Cuppen, H. M., Ioppolo, S., Romanzin, C., Bisschop, S. E., Andersson, S., van Dishoeck, E. F., & Linnartz, H. 2009, A&A, 505, 629

Genzel, R., Ho, P. T. P., Bieging, J., & Downes, D. 1982, ApJ, 259, L103

Gerakines, P. A., Schutte, W. A., Greenberg, J. M., & van Dishoeck, E. F. 1995, A&A, 296, 810

Gibb, E. L., Whittet, D. C. B., Boogert, A. C. A., & Tielens, A. G. G. M. 2004, ApJS, 151, 35

Greene, T. P., Wilking, B. A., Andre, P., Young, E. T., & Lada, C. J. 1994, ApJ, 434, 614

Gürtler, J., Klaas, U., Henning, T., Ábrahám, P., Lemke, D., Schreyer, K., & Lehmann, K. 2002, A&A, 390, 1075

Herzberg, G. 1945, Molecular spectra and molecular structure. Vol.2: Infrared and Raman spectra of polyatomic molecules (New York: Van Nostrand, Reinhold, 1945)

Hidaka, H., Watanabe, N., Shiraki, T., Nagaoka, A., & Kouchi, A. 2004, ApJ, 614, 1124

Hudgins, D. M., Sandford, S. A., Allamandola, L. J., & Tielens, A. G. G. M. 1993, ApJS, 86, 713

Kemper, F., Vriend, W. J., & Tielens, A. G. G. M. 2004, ApJ, 609, 826

Kerkhof, O., Schutte, W. A., & Ehrenfreund, P. 1999, A&A, 346, 990

Kessler-Silacci, J., Augereau, J., Dullemond, C. P., Geers, V., Lahuis, F., Evans, II, N. J., van Dishoeck, E. F., Blake, G. A., Boogert, A. C. A., Brown, J., Jørgensen, J. K., Knez, C., & Pontoppidan, K. M. 2006, ApJ, 639, 275

Lacy, J. H., Faraji, H., Sandford, S. A., & Allamandola, L. J. 1998, ApJ, 501, L105+

Lee, J., Bergin, E. A., & Evans, II, N. J. 2004, ApJ, 617, 360

Min, M., Waters, L. B. F. M., de Koter, A., Hovenier, J. W., Keller, L. P., & Markwick-Kemper, F. 2007, A&A, 462, 667

Moore, M. H. & Hudson, R. L. 1998, Icarus, 135, 518

Muñoz Caro, G. M. & Schutte, W. A. 2003, A&A, 412, 121

Öberg, K. I., Boogert, A. C. A., Pontoppidan, K. M., Blake, G. A., Evans, N. J., Lahuis, F., & van Dishoeck, E. F. 2008, ApJ, 678, 1032

Öberg, K. I., Bottinelli, S., & van Dishoeck, E. F. 2009, A&A, 494, L13

Öberg, K. I., Fraser, H. J., Boogert, A. C. A., Bisschop, S. E., Fuchs, G. W., van Dishoeck, E. F., & Linnartz, H. 2007, A&A, 462, 1187

Osorio, M., Anglada, G., Lizano, S., & D'Alessio, P. 2009, ApJ, 694, 29

Pontoppidan, K. M. 2006, A&A, 453, L47

Pontoppidan, K. M., Boogert, A. C. A., Fraser, H. J., van Dishoeck, E. F., Blake, G. A., Lahuis, F., Öberg, K. I., Evans, II, N. J., & Salyk, C. 2008, ApJ, 678, 1005

Pontoppidan, K. M., Dartois, E., van Dishoeck, E. F., Thi, W.-F., & d'Hendecourt, L. 2003, A&A, 404, L17

Pontoppidan, K. M., van Dishoeck, E. F., & Dartois, E. 2004, A&A, 426, 925

Rodgers, S. D. & Charnley, S. B. 2001, ApJ, 546, 324

Savage, B. D. & Sembach, K. R. 1996, ARA&A, 34, 279

Schutte, W. A. & Khanna, R. K. 2003, A&A, 398, 1049

Schutte, W. A., Tielens, A. G. G., & Sandford, S. A. 1991, ApJ, 382, 523

Skinner, C. J., Tielens, A. G. G. M., Barlow, M. J., & Justtanont, K. 1992, ApJ, 399, L79

Taban, I. M., Schutte, W. A., Pontoppidan, K. M., & van Dishoeck, E. F. 2003, A&A, 399, 169

Tielens, A. G. G. M. & Hagen, W. 1982, A&A, 114, 245

van Broekhuizen, F. A., Keane, J. V., & Schutte, W. A. 2004, A&A, 415, 425

van Broekhuizen, F. A., Pontoppidan, K. M., Fraser, H. J., & van Dishoeck, E. F. 2005, A&A, 441, 249

Watanabe, N. & Kouchi, A. 2002, ApJ, 571, L173

Watson, D. M., Kemper, F., Calvet, N., Keller, L. D., Furlan, E., Hartmann, L., Forrest, W. J., Chen, C. H., Uchida, K. I., Green, J. D., Sargent, B., Sloan, G. C., Herter, T. L., Brandl, B. R., Houck, J. R., Najita, J., D'Alessio, P., Myers, P. C., Barry, D. J., Hall, P., & Morris, P. W. 2004, ApJS, 154, 391